2008-04-20

Transport Studies of Lightly Electron-Doped Manganese Oxides

Corneliu Daniel Chiorescu
University of Miami, cchiorescu@physics.miami.edu

UNIVERSITY OF MIAMI

TRANSPORT STUDIES OF LIGHTLY ELECTRON-DOPED MANGANESE OXIDES

By

Corneliu D. Chiorescu

A DISSERTATION

Submitted to the Faculty
of the University of Miami
in partial fulfillment of the requirements for
the degree of Doctor of Philosophy

Coral Gables, Florida

May 2008

UNIVERSITY OF MIAMI

A dissertation submitted in partial fulfillment of
the requirements for the degree of
Doctor of Philosophy

TRANSPORT STUDIES OF LIGHTLY ELECTRON-DOPED MANGANESE OXIDES

Corneliu D. Chiorescu

Approved:

_____	_____
Dr. Joshua L. Cohn	Dr. Terri A. Scandura
Professor of Physics	Dean of the Graduate School
_____	_____
Dr. Josef Ashkenazi	Dr. Fulin Zuo
Professor of Physics	Professor of Physics

_____
Dr. Francisco Raymo
Professor of Chemistry

CHIORESCU, CORNELIU D. (Ph.D., Physics)

Transport Studies of Lightly Electron-Doped Manganese Oxides (May 2008)

Abstract of a dissertation at the University of Miami.

Dissertation supervised by Professor Joshua L. Cohn
No. of pages in text. (77)

A comprehensive study of transport properties of lightly electron-doped manganese oxides with perovskite structure is presented. Two similar classes are investigated in both their both paramagnetic and antiferromagnetically ordered states: $Ca_{1-x}La_xMnO_3$ and $Ca_{1-y}Sr_yMnO_3$. Much simpler than their widely-studied hole-doped counterparts, these compounds are model systems for investigating the issue of magnetic polaron formation in perovskite manganites. Our measurements sustain the phase segregation scenario both above and below the magnetic ordering temperature in $Ca_{1-x}La_xMnO_3$, but it is found that for $T>T_n$, the small-polaron theory (successful in describing the "colossal" magnetoresistance compounds) is incompatible with our results and a large polaron theory should be used instead. Particularly interesting are the nominally undoped, semiconducting $Ca_{1-y}Sr_yMnO_3$ compounds with a very small electron concentration associated with native oxygen vacancies. At low temperatures, electron bound near vacancies are mobilized in weak applied electric field (F<100 V/cm). This internal current source allows for a distinction between self-trapped and bound magnetic polarons and provides a new tool for studying strongly correlated electron systems with a tunable mobile carrier density.

Acknowledgements

First and foremost I would like express my deepest appreciation to my advisor, Prof. Joshua Cohn, for everything he taught me, for his support and guidance during the past several years. I would also like to thank the committee members, Prof. Ashkenazi, Prof. Zuo and Prof. Raymo for their helpful comments and suggestions regarding this dissertation. Most of the work presented here would have been lot more difficult, if not impossible, without the help of the faculty, staff and fellow graduate students in the Department of Physics, University of Miami. I thank them all.

The financial support provided by the Department of Physics, National Science Foundation under grant No. DMR-0072276 and the Research Corporation (University of Miami) is gratefully acknowledged.

TABLE OF CONTENTS

Chapter 1

Introduction

Condensed matter has always been one the most active research areas in physics. New compounds with exotic new properties involving states with nontrivial spin, charge, lattice and orbital arrangements are being discovered every day. Their rich collection of properties shows a potential for technological applications limited only by one's imagination.

The interest in transition metal oxides and their properties has been triggered by the discovery of high temperature superconductivity in hole-doped cuprates with perovskite structure by Georg Bednorz and Alex Müller in 1986[1]. Broadening of the research efforts to similar materials lead to the discovery of another remarkable property that occurs in cuprates' close relatives, the manganese oxides: the "colossal" magnetoresistance (CMR) effect[2]. These are only two examples of effects that captured the interest of the scientific community in transition metal oxides. Explaining the physics that underlies these intriguing properties became the goal of many scientists, but more than 20 years and 100 000 research papers later (on cuprates alone) this is far from being a closed problem.

The present work focuses on electron-doped manganese oxides. Although the CMR effect has been observed on the hole-doped counterparts, the simplicity of the compounds on the electron-doped side of the phase diagram makes them model systems

for understanding the fundamental properties of transition metal oxides. We explore their properties by means of transport measurements covering a wide range of temperatures.

Chapter 2 of the present work consists of a very brief background on manganese oxides. The large amounts of literature on these compounds, including books and review papers, would make an "in depth" approach superfluous, such that only a brief description of their phase diagram, phenomenology and properties is given.

The third chapter consists of an overview of the quantities measured, followed by a detailed description of the experimental setup and procedures. Details about our particular probes, instruments and data acquisition systems are also given here.

Chapters 4, 5 and *6* discuss experimental data and interpretation and they contain results already published in *Physical Review B*. A magnetotransport study in electron doped $Ca_{1-x}La_xMnO_3$[30] (*Chapter 4*) is followed by a closer look at the paramagnetic phase transport properties in these compounds[17] (*Chapter 5*). *Chapter 6* addresses the slightly different, nominally undoped $Ca_{1-y}Sr_yMnO_3$ class of compounds and the sensitivity of their transport properties to an external electric field[46]. This work ends with a final chapter containing a conclusion and several open questions.

Chapter 2

Background on Manganese Oxides

2.1 Motivation

The plethora of novel effects observed in the magnetic, electronic and structural properties of manganese oxides has attracted much interest from the scientific community in the past ten years. Their remarkable behavior in the presence of relatively small magnetic fields ("colossal" magnetoresistance, CMR) was reported for the first time[3] in the 1950's but the true magnitude of the effect and the potential for technological applications in magnetic storage devices have only been recently realized. The manganite structural and magnetic phase diagrams include phases with unusual spin, charge, lattice and orbital order (see for example Ref [4]). Explaining the complex phenomena that appear as the result of the interplay between these four degrees of freedom has been the subject of intense study.

Competition between various interactions can lead to intrinsic inhomogeneity also known as "electronic phase separation". The study of these inhomogeneities is likely to lead to important information about the physics behind their properties and maybe this information could be extended to explain similar phenomena observed in other transition metal oxide systems such as high-T_c cuprates.

2.2 Crystal and Electronic Structure

Fig. 2.1 shows a cubic perovskite structure ABO_3: the A-site contains a divalent or trivalent large ion such as Ca^{2+}, Sr^{2+}, La^{3+} while the B-sites are occupied by the transition- metal atom, Mn^{3+} or Mn^{4+} for the materials of this study. Six oxygen atoms surround the B-site ion forming MnO_6 octahedron. Substitutions of the divalent atom with a larger one or with a rare earth metal leads to distortion and tilting of the octahedral structure such that the cubic perovskite structure shown in *Fig. 2.1* ends up being orthorhombic or rhombohedral.

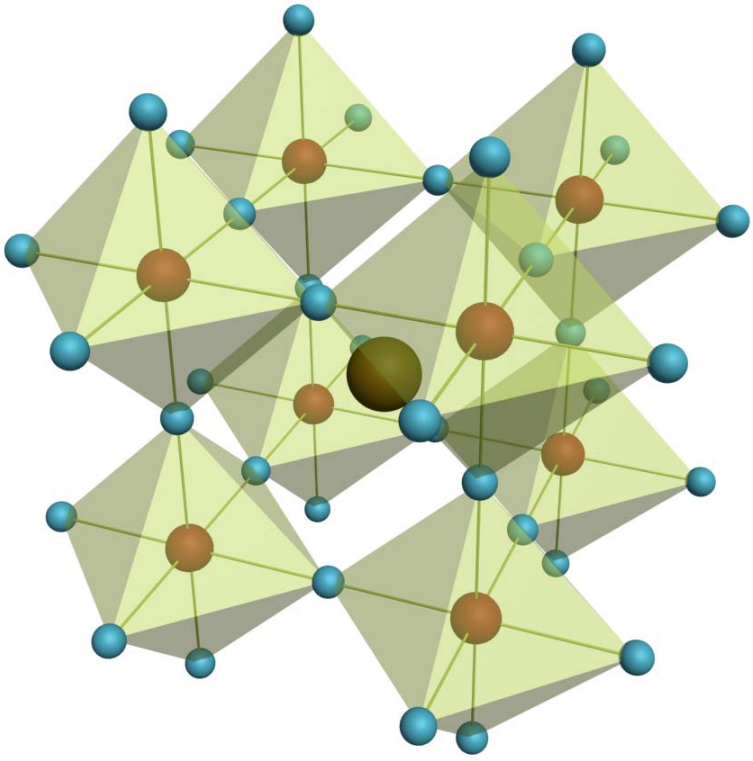

Fig. 2.1 *Perovskite structure and MnO_6 octahedron*

The presence of the six O^{2-} ions surrounding the Mn gives rise to a crystal field potential which affects the free rotation of the electrons by introducing the crystal field splitting of the *d* orbitals: wave functions pointing toward the O^{2-} ion (also known as e_g orbitals) have higher energy then the ones pointing in between them[5,6] (t_{2g} orbitals) (*Fig. 2.2*).

The electron configuration of the Mn ion is dictated by the ferromagnetic Hund coupling of the *3d* electrons. In the case of Mn^{4+} ions, the three d-electrons are localized and they occupy the states of minimum energy: the t_{2g} triplet. Bridged by the O^{2-} ions, the superexchange interaction between the Mn^{4+} ions favors (energetically) an antiferromagnetic alignment of spins throughout the lattice such that the result is a

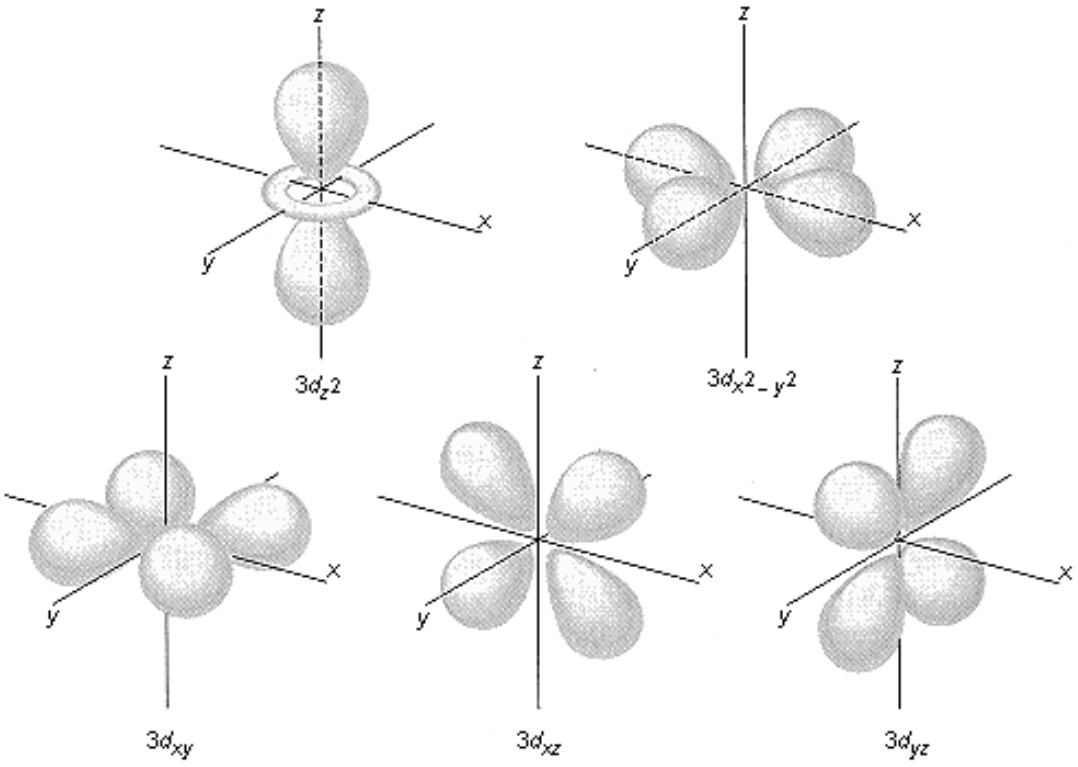

Fig. 2.2 *Crystal field splitting of d orbitals (Ref. [5])*

magnetic configuration in which each spin is antiparallel with the nearest neighbor, the so-called *G-type* antiferromagnetic lattice.

Trivalent substitutions for the A-site ions lead to the appearance of Mn^{3+} ions. The O^{2-} ions surrounding it can slightly readjust their location creating an asymmetry between different directions. This orbital-lattice interaction is called Jahn-Teller effect and effectively removes the degeneracy of the e_g doublet and t_{2g} triplet[6].

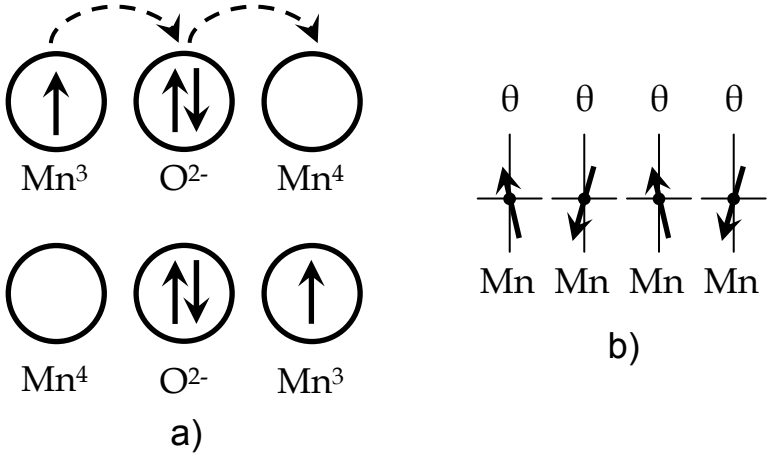

Fig. 2.3 *a) Schematic of double exchange b) spin canted states*

Zener made one of the first attempts to a theoretical study of manganites by explaining their ferromagnetic properties in terms of what is today called *double exchange* interaction (*Fig. 2.3 a*). His explanation was that the ferromagnetism was the result of "indirect coupling between incomplete d-shells via conducting electrons"[7] which can effectively move an electron from a Mn^{3+} to a Mn^{4+} through an O ion, realizing a double exchange of electrons. Zener also mentions the fact that this should not be confused with the superexchange interaction, which would lead to an antiferromagnetic alignment of spins. His work was followed by Anderson and Hasegawa who calculated

the effective electron hopping amplitude as a function of the angle between the spins of the two sites involved in the electron transfer[8].

De Gennes proposed in 1960 a theory[9] regarding the state obtained by doping an antiferromagnetic manganite with electrons or holes. According to him, the result is a spin-canted state (*Fig. 2.3 b*) with a net magnetic moment which could explain the mixed ferromagnetic and antiferromagnetic features observed by experimentalists in manganites physical properties. Contemporary theories indicate that the spin-canted state of De Gennes is unstable against the formation of a "phase separated" ground state consisting of charge-rich (ferromagnetic) and charge-poor (antiferromagnetic) regions of nanoscopic size.

Another theoretical perspective of manganites is Goodenough's analysis of the charge, orbital and spin arrangement in the non-ferromagnetic regimes of the $Ca_xLa_{1-x}MnO_3$ phase diagram[10,11]. His work is based on the notion of *semicovalent exchange* in which Coulomb interactions and oxygen ions play a key role and which can lead to both ferromagnetic and antiferromagnetic coupling between Mn ions, depending on the orientation of their occupied e_g orbitals. Although there is still debate over Goodenough's model, it is clear that he was the first one to point out the importance of orbital ordering in manganites.

2.3 Lightly Electron-Doped Manganese Oxides

Substituting the alkali-earth metal in an undoped G-type antiferromagnetic manganese oxide such as $CaMnO_3$ with a trivalent rare-earth species introduces extra electrons and thus Jahn-Teller active Mn^{3+} ions into the lattice. In this doping regime their concentration remains far below the threshold for which complex electron correlation effects like charge and orbital order take place but their presence leads to some very interesting effects, some of which will be discussed in the following chapters. The simplicity of these compounds coupled with the possibility of extending some of the results to the much more complex hole doped counterparts have attracted considerable interest in their physical properties.

Magnetization measurements in $Ca_xLa_{1-x}MnO_3$ show that a small ferromagnetic moment develops in these compounds below the antiferromagnetic transition temperature T_N and increases with increasing electron doping for $x \leq 0.05$[12]. Recent neutron scattering studies[13,14] seem to sustain the phase segregation scenario (phenomenon observed for the first time in the hole-doped compounds): within the antiferromagnetic background of the parent compound, ferromagnetic droplets of nanometric size increase in density with increasing x. These studies also postulate that a crossover region near x=0.02 marks the transition between isolated FM droplets to the long range spin canted state that appears for $x \geq 0.06$.

Another class of manganese oxides that has been the subject of our research efforts for the past few years is the $Sr_yCa_{1-y}MnO_3$ series. Although nominally undoped, these compounds have a small electron concentration associated with oxygen vacancies.

Each of these vacancies liberates two electrons creating two Mn^{3+} ions which leads to an effective electron concentration of 10^{18} cm^{-3} = 10^{-3}~10^{-4} electrons per formula unit. The isovalent Sr substitutions for Ca increases the Mn-O-Mn bond angle, θ, toward 180° such that the crystalline structure of these compounds changes from orthorhombic for $y \leq 0.6$ to tetragonal ($0.6 \leq y \leq 0.8$) and to cubic for $y \geq 0.8$[13]. The same study of Chmaissem *et al.* (*Ref. [15])* points out that the ordering temperature increases with increasing y in the orthorhombic phase and varies linearly with $\langle \cos^2 \theta \rangle$ (*Fig. 2.4*).

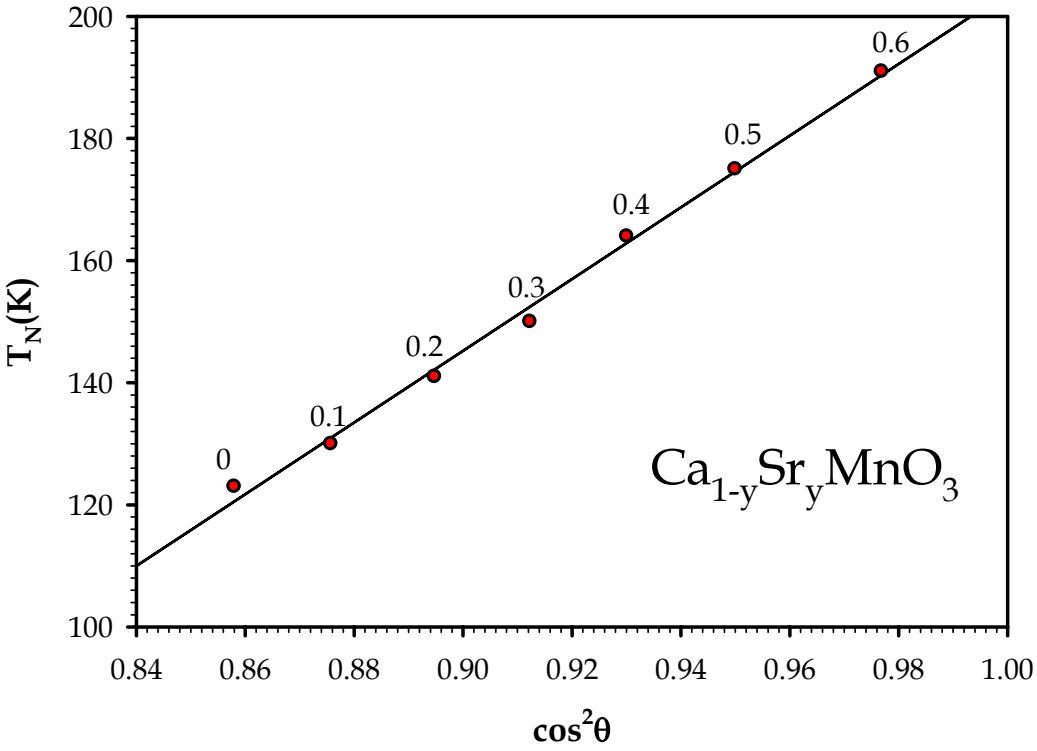

Fig. 2.4 *Dependence of T_N with the Mn-O-Mn bond angle*

.

Chapter 3

Experimental Considerations

3.1. Transport Coefficients

3.1.1. Electrical Resistivity (ρ)

The experimental setup for resistivity measurements is shown in *Fig. 3.1*: a four wire measurement is employed in order to eliminate parasite resistances generated by contacts and wires. To further enhance the accuracy of our measurements, multiple

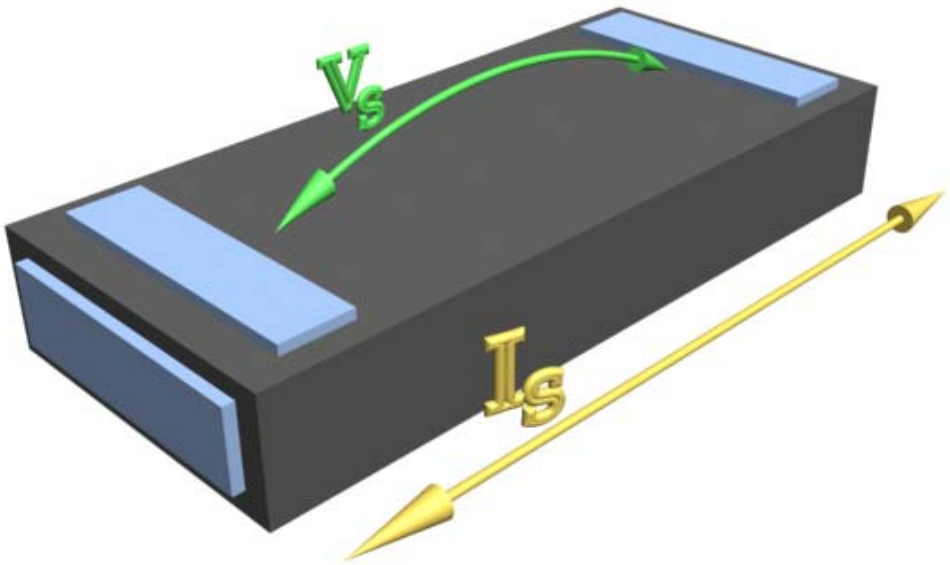

Fig. 3.1 *Experimental setup for resistivity measurements*

readings of the sample voltage are averaged (40-100 for each direction of the current flowing through the sample). The resistivity is then calculated using the well known formula:

$$\rho\langle\Omega cm\rangle = R\frac{S}{l} \tag{3.1}$$

where R is the resistance of the sample, S is the cross-sectional area and l is the distance between the voltage contacts.

For resistivity versus electric field measurements, the Joule heating of the sample for the higher values of the applied current has to be taken into account. In this case, the sample is varnished down onto the stage and the sample's temperature is monitored directly using a thermocouple.

3.1.2. Thermal Conductivity (κ)

The *steady state technique*[16] used to measure thermal conductivity is shown schematically in *Fig. 3.2*: a 1 KΩ surface mounted resistor is used to generate a temperature gradient along the sample. The specimen is thermally linked to a thermal sink at the other end by attaching it to a copper tab (or sapphire crystal) with silver epoxy. The temperature difference is measured using a 25 μm (0.001") diameter *type-E* (chromel-constantan) differential thermocouple. Another thermocouple is used to measure the average temperature increase of the sample relative to the thermal sink. The thermal conductivity is given by:

$$\kappa\left\langle\frac{W}{m\cdot K}\right\rangle = \frac{P}{\Delta T}\frac{l}{S} \tag{3.2}$$

where P is the heater power required to generate a temperature difference ΔT between two points separated by l along a sample with crossectional area S.

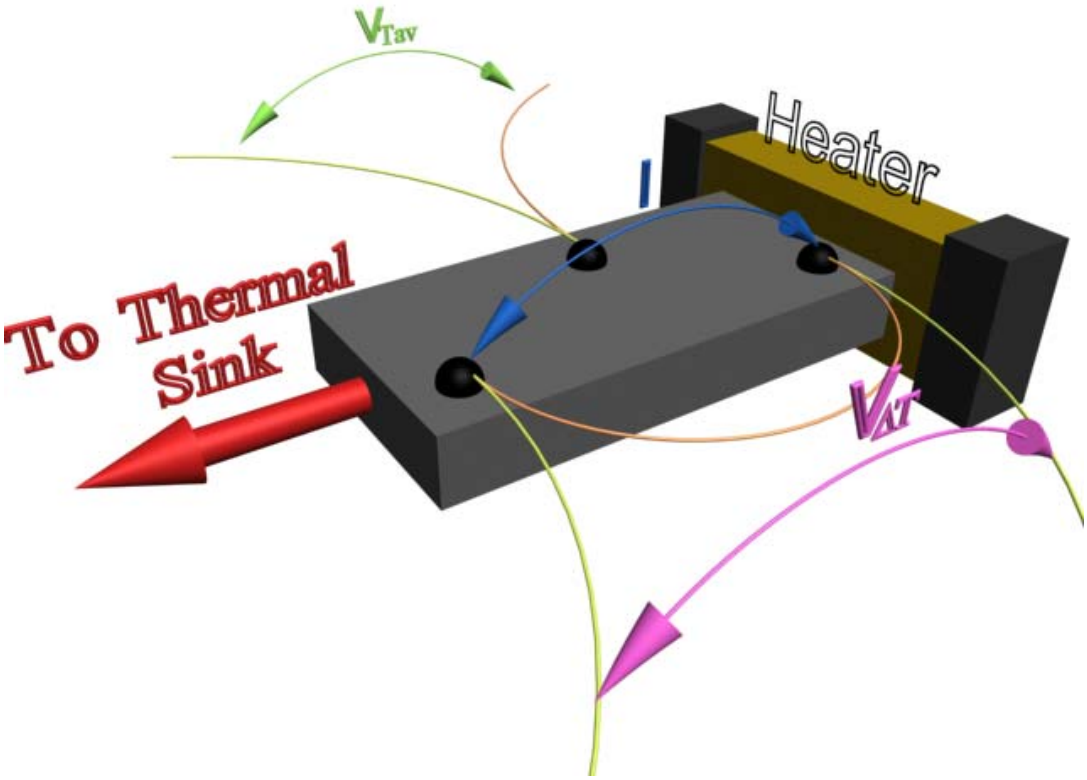

Fig. 3.2 *Experimental setup for thermal conductivity measurements*

There are several precautions that need to be taken when doing a thermal conductivity measurement and all of them address issues related to various heat losses that could occur through convection, conduction and radiation. While convection losses are virtually eliminated in a well pumped cryostat, the conduction through the wires can be minimized by choosing long, resistive leads (we typically use 0.001" constantan) for the "hot" contacts: heater voltage and current and "hot" sample current.

The radiation losses can be substantial at higher temperatures but they can be either estimated[24] or measured and the data corrected for errors.

An estimation of radiative losses is done as follows: starting with Stefan-Boltzmann law, the radiation loss between the sample and the surroundings is given by:

$$P_{loss}^{rad} = \varepsilon \sigma_{SB} A \left(T_S^4 - T_B^4 \right)$$

Where ε is the emissivity ($0<\varepsilon<1$), σ_{SB}=5.7x10^{-8} W/m^{2}K^4 is the Stefan-Boltzmann constant, A is the cross sectional area, T_S is the temperature of the sample and T_B is the temperature of the surrounding background. If $\Delta T = T_S - T_B$ is small, a Taylor expansion (in which the higher order terms were neglected) of the above relation leads to:

$$P_{loss}^{rad} \propto T^3 \Delta T$$

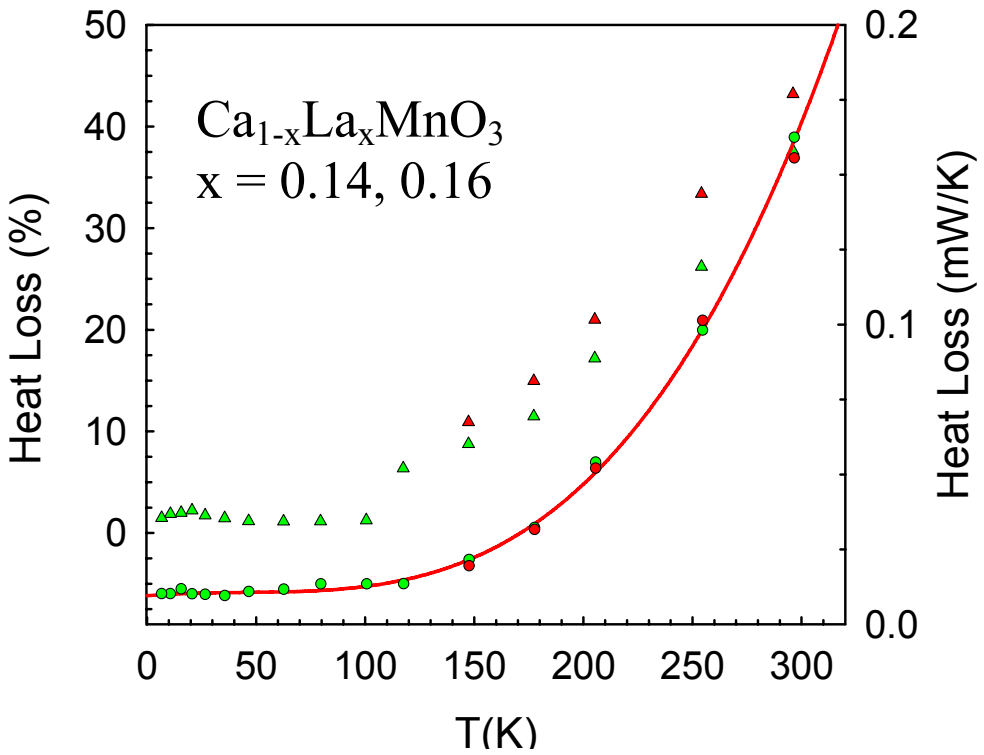

Fig. 3.3 *Example of measured radiation loss for two polycrystalline $Ca_xLa_{1-x}MnO_3$ sample, x=0.14 (red), 0.16 (green). Circles represent the losses in W/mK (right ordinate), triangles in percents (left ordinate)*

Estimating the heat losses can be done as described above, as a simple sum of conduction and radiation terms, or it can actually be measured. The way to do this is to disconnect the sample from the heatsink and, for certain temperatures at which $\kappa(T)$ has already been measured, adjust the heater power by trial and error until the average temperature of the sample is raised by the same amount as during the $\kappa(T)$ measurement. It can be easily shown that the heater power required to do this is the total heat lost (through convection, conduction and radiation).

As previously mentioned, the dependence with T^3 makes radiation losses problematic at high temperature but they are negligible at low temperatures. Radiation shielding and choosing a short, fat sample for such an experiment also helps minimizing these losses. *Fig. 3.3* shows measured heat losses for two different $Ca_xLa_{1-x}MnO_3$ specimens (x=0.14, 0.16). For these two samples, the radiation losses expressed as a percentage of the measured κ show clearly that radiation correction near room temperature can be as high as 15-20%.

3.1.3. Thermoelectric Power (S)

The experimental setup is very similar to the one used for measuring thermal conductivity, the only difference being the addition of two gold leads to measure the sample voltage (*Fig. 3.4*). The thermoelectric power (thermopower, TEP) is given by:

$$S\left\langle \frac{\mu V}{K} \right\rangle = \frac{V_S}{\Delta T} \tag{3.3}$$

where V_S is the sample voltage due to a temperature difference ΔT. It should be noted that some geometrical corrections have to be taken into account when the distance between the voltage contacts (l_V) and thermocouple junctions ($l_{\Delta T}$) are not the same. In general the

differential thermocouple is place right on top of the voltage contacts, like in *Fig. 3.4*, but this is not always possible. Such is the case of extremely small samples (*Fig. 3.7*) where space constraints force a different location for the two pairs of contacts.

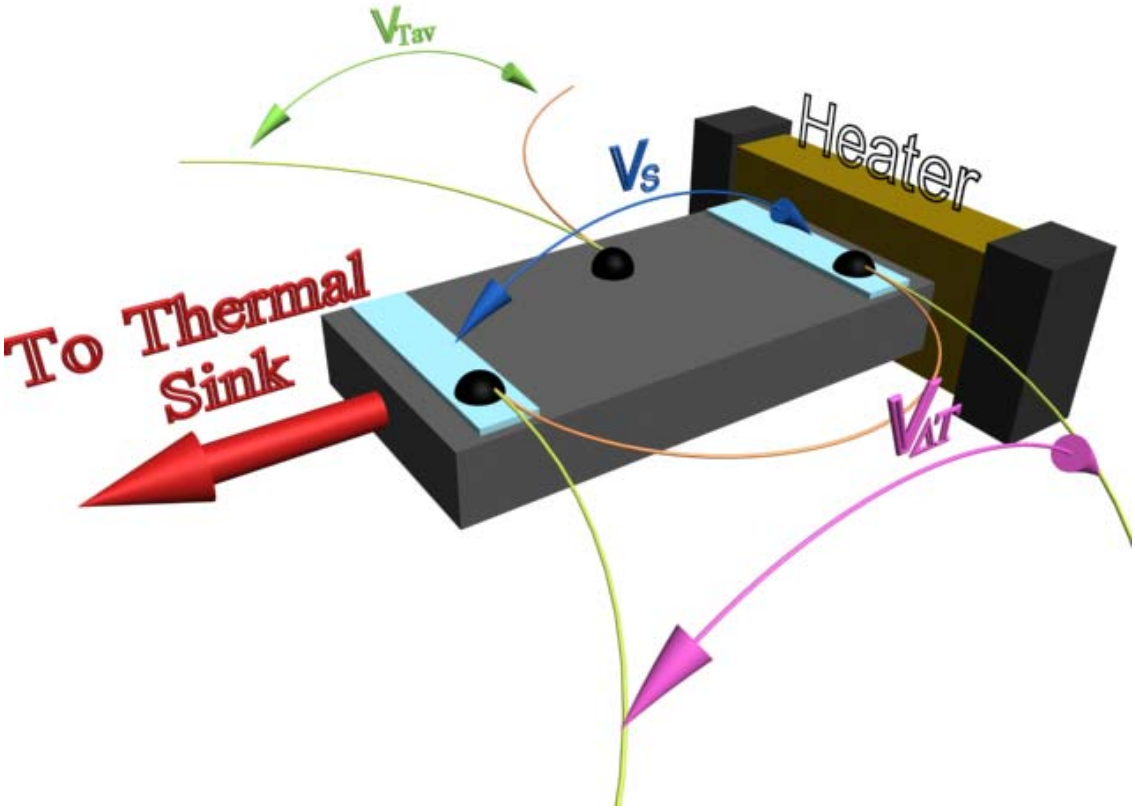

Fig. 3.4 *Experimental setup for thermopower measurements*

The measured thermopower is the difference between that of the specimen and that of the lead wires (*Fig. 3.5*), so that the specimen thermopower must be computed by subtracting the T-dependent calibration of the lead TEP. In the present studies on semiconductor specimens with large thermoelectric power, this correction constitutes less than 1%.

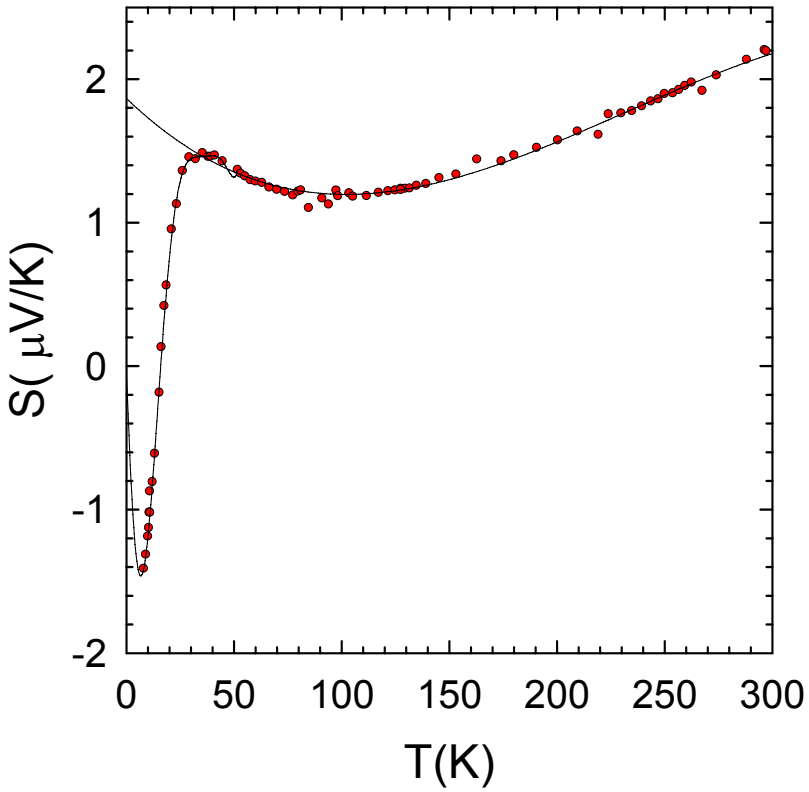

Fig. 3.5 *Thermopower of 0.001" gold wire*

3.1.4. Actual Experimental Setup and Procedure for *κ, ρ, S* Measurements

The measurement techniques were described above more from a theoretical point of view. Our typical experiment consists of temperature (4-300K) and/or sample current (10mA-5nA) sweeps, so a considerable amount of time can be saved if the samples are wired for *simultaneous measurements of κ, ρ, S.* Our usual choice is to make all these measurements such that our actual experimental setup looks like the one described in *Fig. 3.6*.

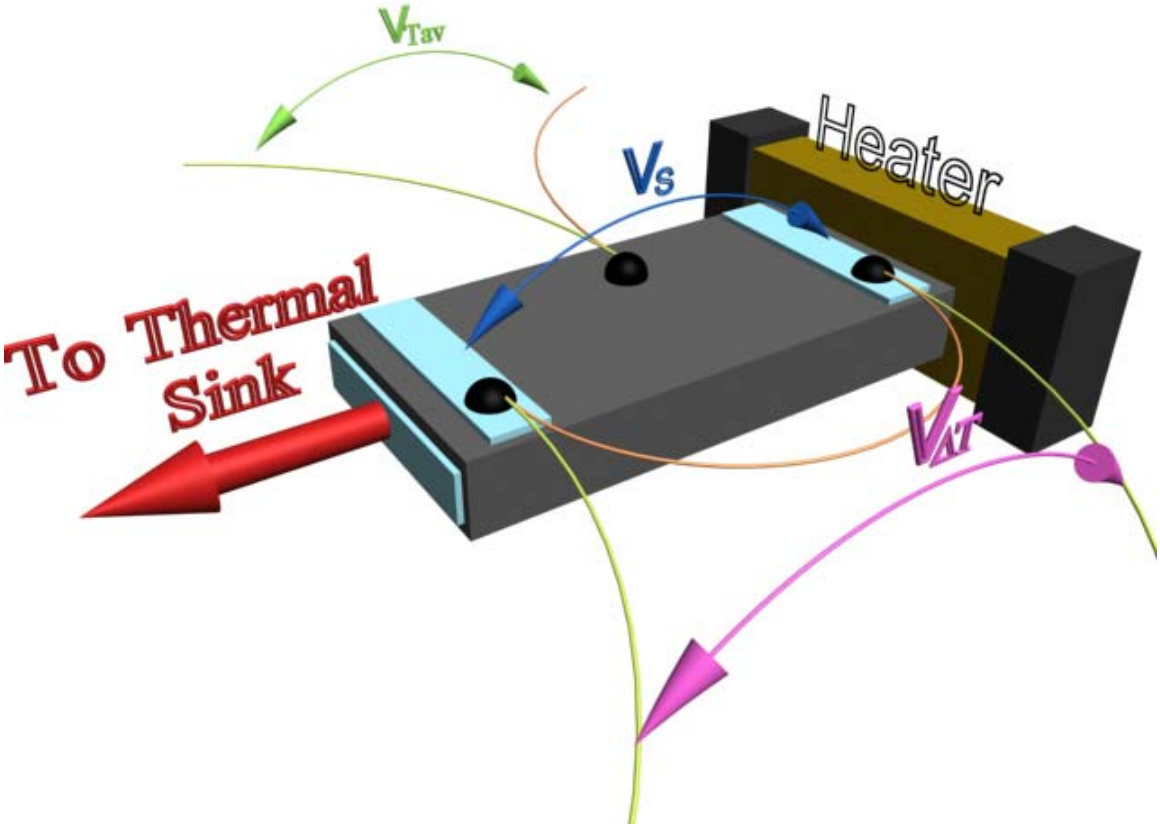

Fig. 3.6 *Experimental setup for κ, ρ, S measurements*

Fig. 3.7 shows an actual sample mounted for a *κ, ρ, S* measurement. This particular sample has $\sim 0.8 \times 0.5 \times 0.1$ mm^3 and due to its small dimensions, the wire configuration is slightly different than the one described above.

The first step in preparing such a sample for measurement is applying electrical contacts for a four-wire measurement using silver paint or epoxy: current (left hand side, coming from underneath the heater and right hand side attached to the thermal sink) and voltage (copper wires on the bottom side of the sample). The sample is then attached using silver epoxy to a sapphire crystal thermally linked to the sample stage. The next

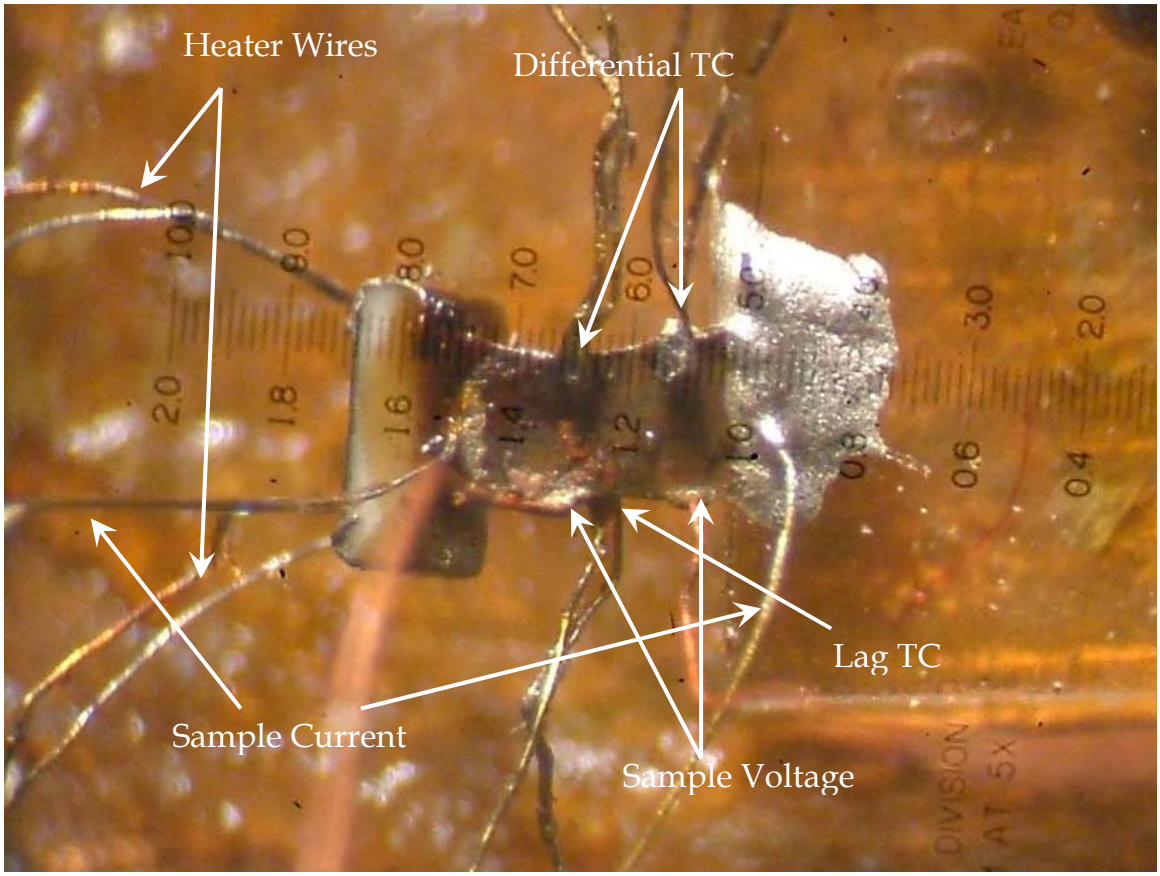

Fig. 3.7 *Actual sample of approximate dimensions* $\sim 0.8 \times 0.5 \times 0.1$ mm^3 *mounted for k, ρ, S measurement. Each small division of the scale represents 0.0286 mm*

step is attaching the two thermocouples using a thermally conductive varnish or epoxy: the differential one (top side) and the lag temperature thermocouple, in this case mounted underneath the sample (bottom side) due to space constraints. The last step is attaching the heater. Due to high risk of shorting the heater contacts to the "hot" current contact, varnish is preferred for this operation as it can be easily removed with ethanol and reapplied if needed.

3.2 Hall Effect and Magnetoresistance

In general, the physics involved in the Hall effect is straight forward: when a magnetic field is applied perpendicular to the current flowing through a sample, the Lorentz force acting on the charge carriers creates a concentration gradient across the sample. The electric field that arises due to this gradient is called the *Hall field* and it opposes further deflection such that, in steady state, the current lines are again parallel to the longitudinal axis. The Hall coefficient is defined as the constant of proportionality between the Hall field and the product *JH*:

$$R_H = \frac{E_y}{j_x H} = \ldots = -\frac{1}{ne} \tag{3.4}$$

The Hall measurement is widely accepted as one of the most accurate methods to determine the effective carrier concentration.

Things become more complicated in materials showing a high magnetization due to strong, localized magnetic moments. In these materials, one might expect the same type of linear dependence of E_H versus H with R given by the value of the slope. But the observed behavior of such a material (a ferromagnet, for example) is quite different and it is shown schematically in *Fig. 3.8:* the Hall resistivity ρ_H versus magnetic field plot consists of two linear portions of different slope; this change in slope cannot be attributed entirely to the Lorentz force. The curve shown below can be fitted empirically with the formula:

$$\rho_H = R_0 H + R_1 M \tag{3.5}$$

Where the first term is responsible for the ordinary Hall effect while the second,

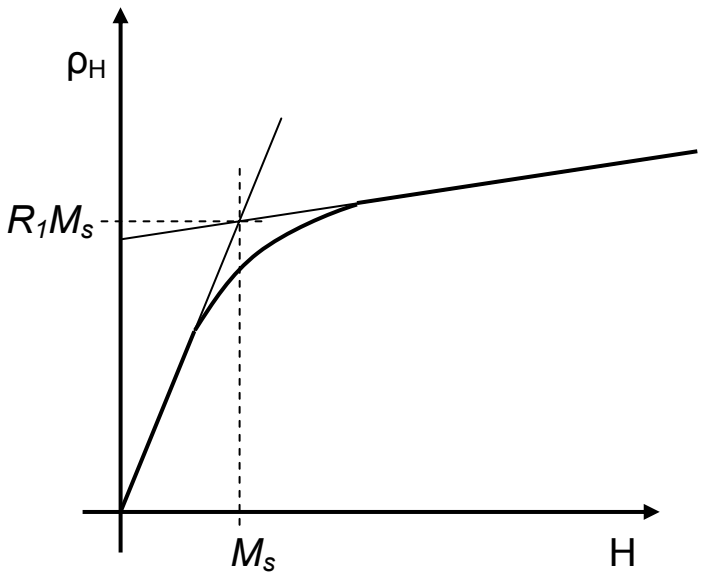

Fig. 3.8 *Hall resistivity versus magnetic field for a magnetic material*

containing the spontaneous magnetization *M*, represents an anomalous contribution (with the constant R_1 known as the anomalous Hall coefficient). The phenomenon has become known as the *anomalous Hall effect* and a consensus regarding its origins has yet to be reached by the scientific community. It is attributed to either spin dependent scattering of the charge carriers[47] (disorder-related) or it is sometimes described in terms of Berry phase effect in the crystal momentum space[48].

Magnetoresistance and Hall measurements are usually done simultaneously and the experimental setup looks like the one described in *Fig. 3.9*: current flows along the sample while a magnetic field is applied perpendicular to it. The Hall voltage develops across (perpendicular to both current and magnetic field) while the sample voltage is read along the sample.

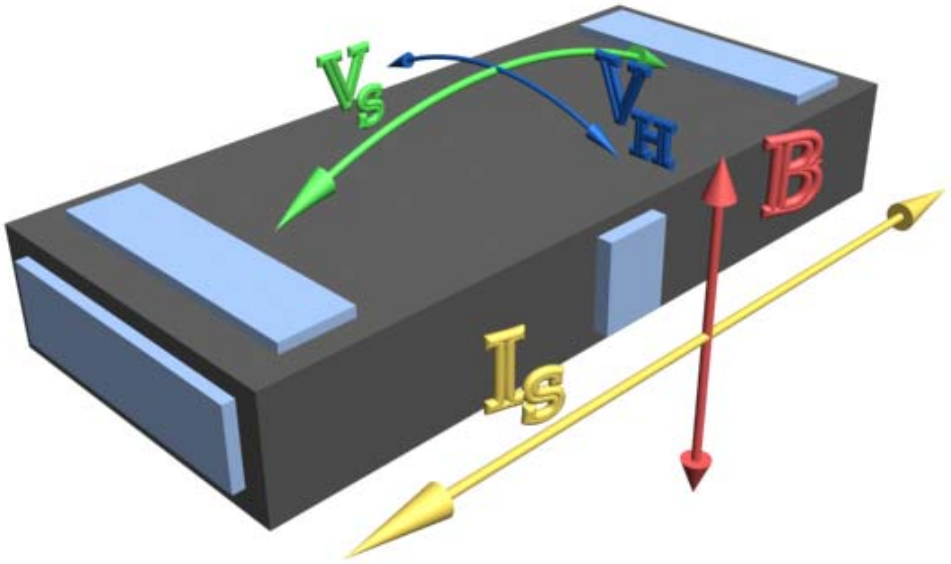

Fig. 3.9 *Hall effect and magnetoresistance experimental setup*

An ideal Hall specimen has to be extremely thin in order to maximize the measured signal since the Hall voltage is inversely proportional to the thickness of the specimen. But probably the biggest source of errors in a Hall measurement is the inherent misalignment of the Hall contacts which creates a parasite *longitudinal* potential difference due to the current applied through the sample. To correct the data for this error, both current and field reversal are employed such that in the end the Hall voltage is calculated using:

$$V_H = \frac{1}{4}\left(V_{I+B+} + V_{I-B-} - V_{I-B+} - V_{I+B-}\right)$$

3.3 Materials and Techniques

Our typical measurements are done in a wide range of temperatures, electric and magnetic fields. While different experiments require different experimental setups, there are several materials and techniques that are used in almost all of them.

The preparation method for the *samples* we have studied, both mono- and polycrystals is described elsewhere[12,15,17]. Their dimensions are in general given by the quantities we want to measure: a very thin sample is required for accurate Hall measurements since the Hall voltage is inversely proportional to the thickness of the sample, but such a sample would not be suitable for thermal conductivity measurements where a short, fat specimen is preferred.

The application of *electrical contacts* is arguably the most important and most time consuming part involved in preparing a sample for measurement. Almost always done at the microscope using fine, non-magnetic tweezers, this operation consists of attaching 0.001" fine wires to the sample using silver paints and epoxies. By far, the biggest problem we usually run across during this process is the contact resistance that develops at the interface between the metal (silver) and the sample surface caused by the difference between the Fermi levels of the two materials. Annealing the contacts can sometimes reduce this resistance, but it can still cause problems like noisy readings and, since this resistance increases exponentially with the temperature, it can limit the temperature range.

Thermocouples are another vital component of our experiments. They are made in our lab by welding together 0.001" chromel and constantan wire (*type-E*) and they can be

either differential or "average temperature" thermocouples. The differential thermocouples have two junctions and are used to measure the temperature gradient along the sample for thermopower or thermal conductivity measurements. The average temperature (lag) thermocouple has only one junction and, as the name suggests, it is used to measure the average temperature drift of the sample relative to the stage. *Fig. 3.10* shows a plot of the thermoelectric voltage of a type-E thermocouple as a function of temperature.

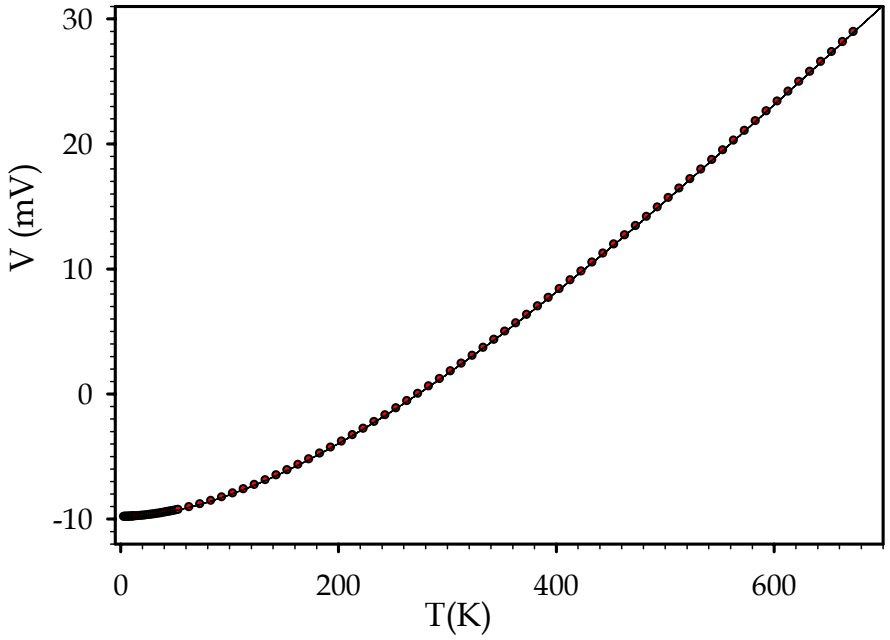

Fig. 3.10 *Type-E thermocouple data from NIST ITS-90 Thermocouple Database (www.nist.gov)*

The type of *thermometer* we use on a particular experiment is strongly dependent on the temperature interval and whether we have a magnetic field present or not. In general, for κ, ρ, S measurements we use platinum above 30K because of its high sensitivity and large calibration interval. For low temperature we use Germanium sensors while their low

magnetoresistance makes Cernox sensors ideal for Hall measurements. The diode is surface mounted which makes it an excellent "all around" choice or when experimenting with various experimental setups and stages as it can be easily mounted or removed.

Sensor	***Calibration range***	***Performance in magnetic field***
Platinum	15-900K	Fair above 30K
Silicon Diode	1.4-500K	Fair above 60K
Germanium	0.05-100K	Not recommended
Cernox	0.1-325K	Excellent

3.4 Cryostats and Magnet System

For κ, ρ, S measurements we have been using a ^{3}He cryostat for storage dewars described in detail in *Ref. [18]*. The basic principle of operation consists of two similar cooling stages: the first one is a continuously filled ^{4}He pot that is kept at 1.5K through cryopumping (a small mechanical pump is usually enough to bring it at this temperature). The purpose of this first stage is to generate a temperature low enough for the ^{3}He to condense. ^{3}He is absorbed into a charcoal volume and once 1.5K is reached, turning on a heater liberates it. In contact with the ^{4}He pot, it liquefies and drips into a secondary pot, eventually bringing this one to 1.5K also. Cooling of this secondary pot down to 0.35K is done by turning off the heater on the charcoal pump and thus cryopumping the ^{3}He back

into the charcoal volume. Besides the ability of this cryostat to go to very low temperatures, one of its biggest advantages is the sealed ^{3}He system and the excellent radiation shielding which makes it ideal for heat transport measurements.

If we remove the cooling stages described above we will have a pretty good image of our secondary cryostat. This particular cryostat is used mostly for magnetoresistance and Hall measurements and while better radiation shielding could be beneficial for temperature stabilization, this is not a critical matter since the magnet system it was designed for has a secondary temperature stabilization system for the sample insert (in addition to the one we already have on the stage).

For magnetotransport measurements we used a superconducting magnet made by JANIS*:* their "OptiMag" system equipped with a "SuperVariTemp" sample insert. The NbTi Helmholtz coils are capable of fields of up to 9T ± 0.1% over 1cm for magnet currents of 80A (supplied by a Power Ten power supply, model 3300D-10100). The magnet's power supply controller (American Magnetics, Model 412) was interfaced with a PC through a Keithley DAC-02 analog output board (2 channel, 12 bit), such that the magnet operation is almost fully automated. "Almost" because this particular magnet system did not come with a current reversal switch, changing the direction of the field is done by physically switching the power leads.

The temperature inside the sample insert is controlled by modifying the amount of liquid helium allowed to enter through a needle valve (that communicates with the helium reservoir) and the power of a heater that vaporizes this liquid helium (vaporizer).

3.5 Data Acquisition and Instruments

Our experiments – with very few exceptions – are fully automated: we use a computer to control the operation of our instruments through GPIB and data acquisition cards and, after the initial parameter input, most of them don't require operator presence. The data acquisition software used was designed by our research group using *VISUAL BASIC* (κ, ρ, S measurements) and *LABVIEW* (Hall effect and magnetoresistance, thermometry).

The way the data is taken is standard: all our programs contain an initialization sequence that ensures the proper communication with the instruments, sets up optimal parameters for that particular experiment and creates the output files. The temperature is set through a temperature stabilization sequence: the temperature is read continuously and plotted as a function of time, then the slope of this plot is constrained to a certain value depending on the type of experiment and the temperature sensor.

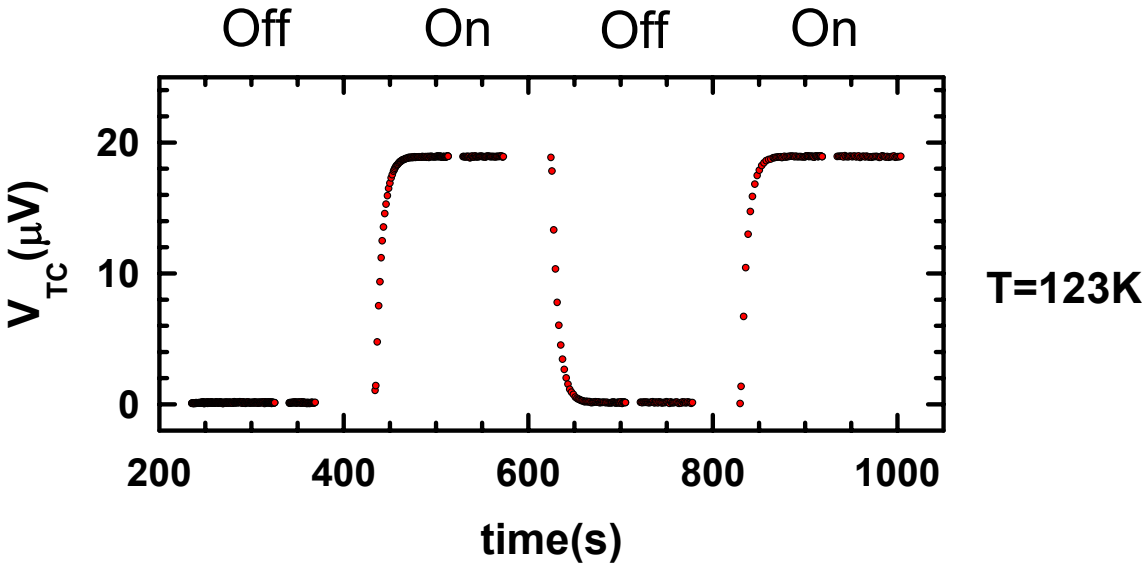

Fig. 3.11 *Heater cycling in a thermal conductivity/thermopower measurement*

Once finished, this sequence is repeated after a 30 seconds delay in order to detect any small temperature drifts that can affect our readings (since data acquisition can take 10-20 minutes). Data acquisition sequence is next: multiple readings of the various voltages are averaged to ensure the accuracy of our results. Due to their extreme sensitivity to the variations of external parameters, even more precautions are taken in the case of thermal conductivity and thermopower: the heater is cycled twice and κ, S are measured for both "Off" and "On" heater power (after making sure that the sample has reached equilibrium – see *Fig. 3.11*). If more than one sample is being measured, this sequence is repeated for each of them. After the last step (recording the data and plotting the graphs) the cycle begins again for the next temperature.

The various instruments used in our experiments are shown in the table below:

Instrument	*Manufacturer and Model*
Temperature controller	Lakeshore DRC-91CA
Digital voltmeter	Keithley 182
Current source	Keithley 224
Voltage source	Keithley 230
Scanner	Keithley 705
Electrometer	Keithley 6512

Chapter 4

Magnetic Inhomogeneity and Magnetotransport in Electron-Doped $Ca_{1-x}La_xMnO_3$

4.1 Electronic Phase Separation

Over the past several years it has become clear that explaining the physics behind the large number of novel effects observed in strongly correlated electron systems is not possible without understanding the concept of "electronic phase separation".

It has been proven that the canted spin structures that were used by De Gennes[9] to explain the ferromagnetism observed in manganites are not stable for realistic antiferromagnetic coupling strengths. A "separated state" consisting of ferromagnetic clusters embedded in the antiferromagentic matrix of the parent compound emerges as an intrinsic consequence of the competion between double exchange and superexchange interactions between magnetic ions. Such a behavior has been observed in both lightly hole doped[19,20] and lightly electron doped[12,21] manganese oxides.

As noted in *Section 2.3,* $CaMnO_3$ is a G-type antiferromagnet with T_N=125 K. Trivalent rare-earth substitutions for Ca introduce Mn^{3+} ions in the antiferromagnetic matrix of the parent compound. Magnetization[12] measurements on lightly electron doped manganese oxides show a small ferromagnetic component to the low-T saturation magnetization which grows with La doping in $Ca_{1-x}La_xMnO_3$. This work focuses on the

physics underlying the change in behavior evident as a slope change clearly visible in the saturation magnetization versus electron concentration plot (*Fig. 4.1*).

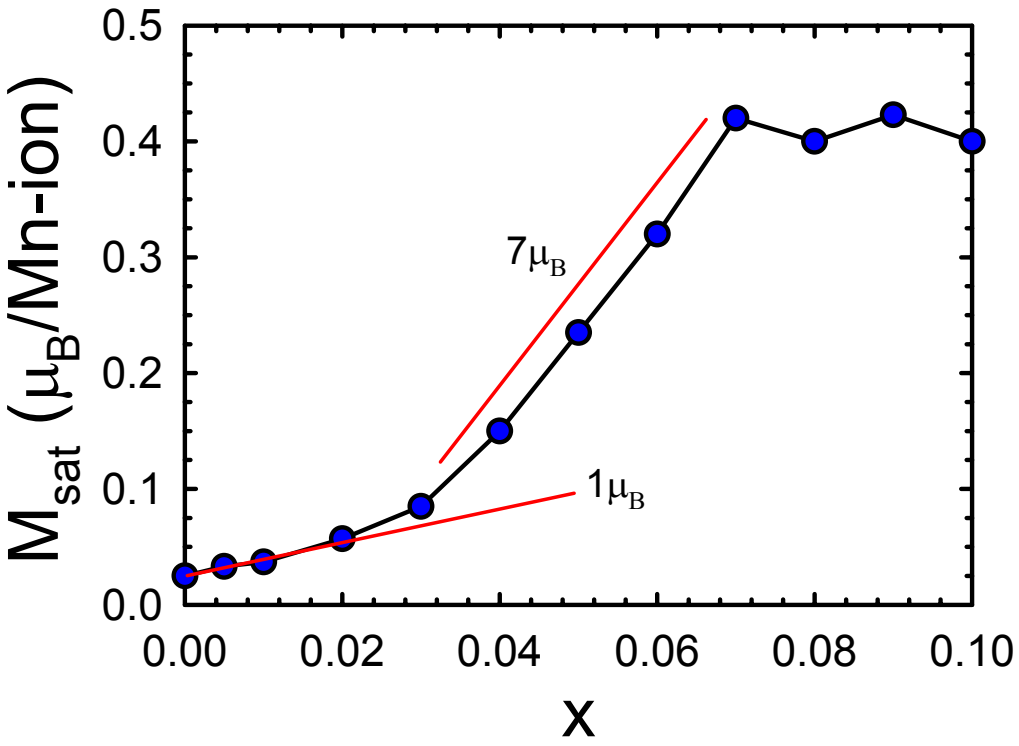

Fig. 4.1 *$Ca_{1-x}La_xMnO_3$: Saturation Magnetization vs x at T=5K*[12]

Neutron scattering[13,14] studies bring further evidence to the phase segregation scenario. These studies seem to suggest that seven-site ferromagnetic polarons induced by electron doping increase in concentration with increasing x. For $x \geq 0.06$ this state changes to a long range spin-canted state and it has been postulated in these studies that $x = 0.02$ marks a crossover region from isolated clusters to long range spin canted state and that both structures coexist in between the two. This transition is the object of our magnetotransport study in $Ca_{1-x}La_xMnO_3$. Another objective of this study is to investigate

whether the paramagnetic phase magnetoresistance follows the proportionality with $(M/M_S)^2$ reported in the "colossal" magnetoresistance hole doped counterparts[22].

4.2 Results and Analysis

4.2.1. Magnetization

Fig. 4.2 (a) shows the $T=5K$ magnetization as a function of magnetic field for several electron doped $Ca_{1-x}La_xMnO_3$ polycrystalline compositions measured in fields of up to 8T. For lower doping levels ($x \leq 0.02$), these curves show a behavior typical to a superposition of two components: a ferromagnetic one that saturates at $H \sim 1$ T and a linear one corresponding to the antiferromagnetic lattice background. As the doping increases above $x \geq 0.04$ the dependence of the magnetization with the applied field changes drastically: the saturation is no longer obvious, implying that the ferromagnetic contribution changes throughout the field range. This behavior is more clearly shown in *Fig. 4.2 (b)* where $\chi = dM/dH$ was plotted against the applied field. It can be clearly seen here that above the saturation field for reorienting the ferromagnetic domains (H=2T) dM/dH becomes independent of the applied field for $x < 0.02$ and strongly field dependent throughout the field range for $x \geq 0.04$. For x=0.03 we see features shared from both types of behavior: dM/dH saturates quickly, it shows a linear region (2-4 T) that is nearly independent of the applied field and it becomes more field dependent as the H increases toward 8 T.

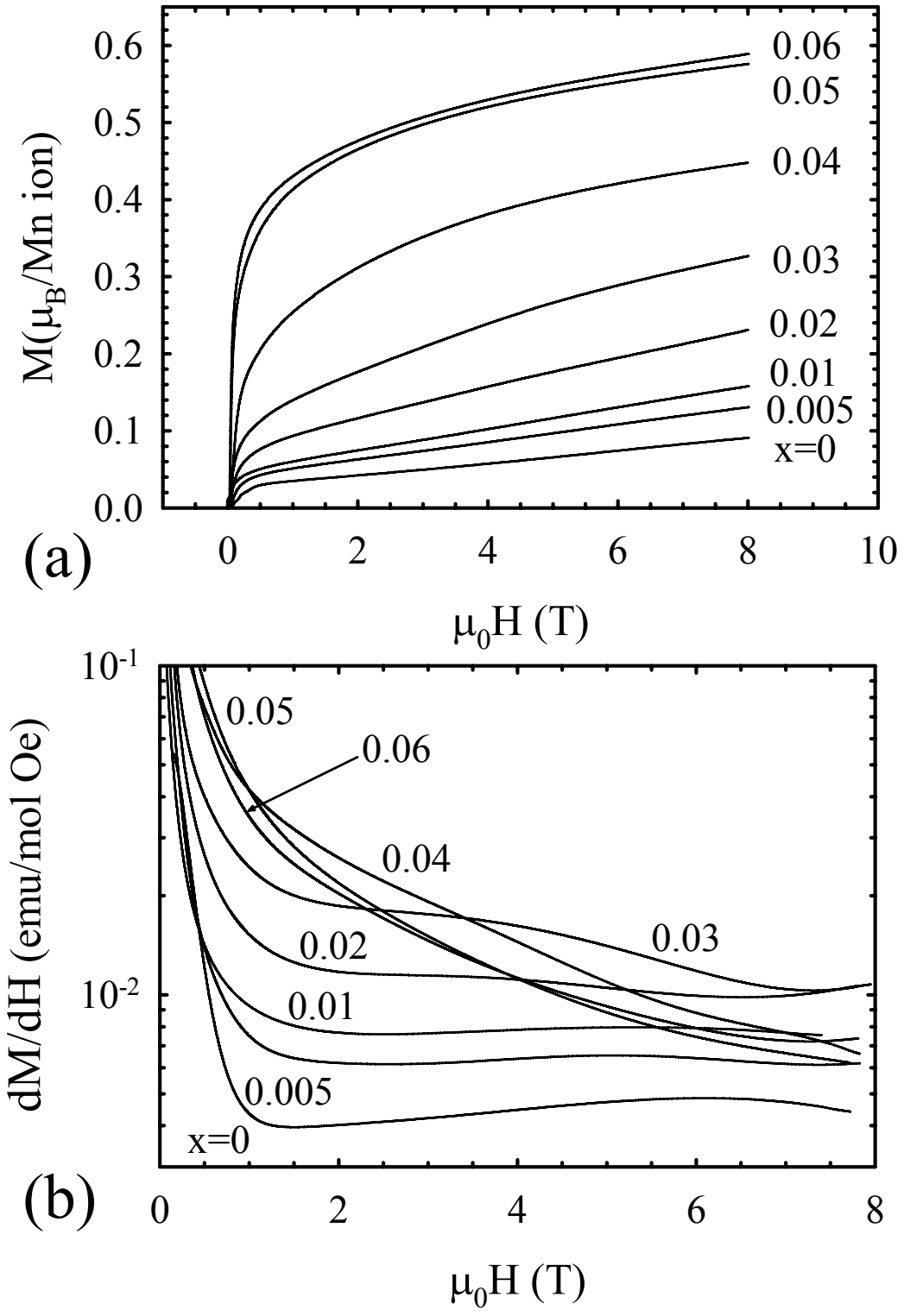

Fig. 4.2 *$Ca_{1-x}La_xMnO_3$: Magnetization (a) and susceptibility (b) vs field*

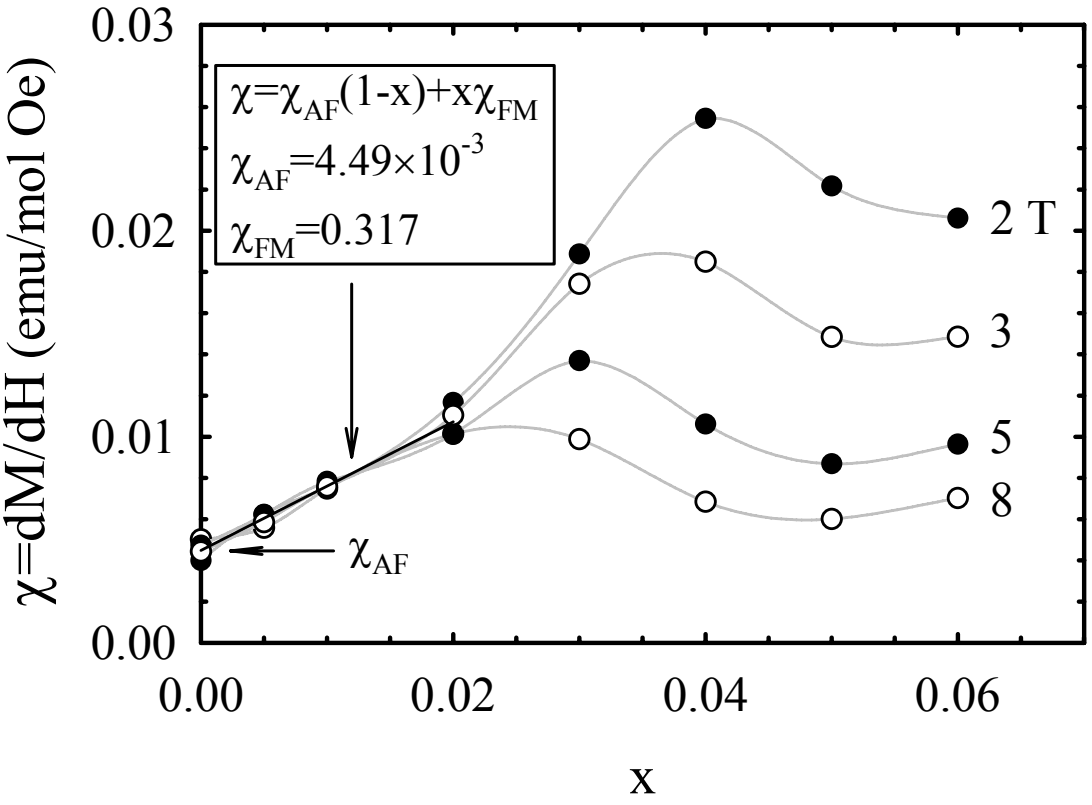

Fig. 4.3 *Magnetic susceptibility versus doping*

The crossover region near *x=0.02* suggested by the change in magnetization's behavior is more visible in *Fig. 4.3* where χ is plotted as a function of *x* for several values of the magnetic field.

If the ferromagnetic contribution to the magnetizations is caused by ferromagnetic droplets and/or spin canted clusters, the linear region of χ versus *x* plot, presumably representing a regime for which these structures do not interact, can be modeled as a sum of two components[23]: one proportional to the number of doping electrons, *x,* representing the contribution to the total magnetization of these droplets, and a second component which represents the antiferromagnetic contribution of the background:

$$\chi = \chi_{AF}(1-x) + x\chi_{FM} \tag{4.1}$$

Applying this model to our particular case (*Fig. 4.3*) yields $\chi_{AF}=4.49\text{x}10^{-3}$ emu/mol Oe. The value for $\chi_{AF}=0.317$ *emu/mol Oe*$=0.57\ \mu_B$*/Mn ion kOe* corresponds to the increase of magnetization by one spin polarized electron per each doped electron in 20 kOe of external field.

4.2.2 Low temperature resistivity

Previously published studies of lightly electron doped manganese oxides establish these compounds as heavily doped, n-type semiconductors. In the low temperature range,

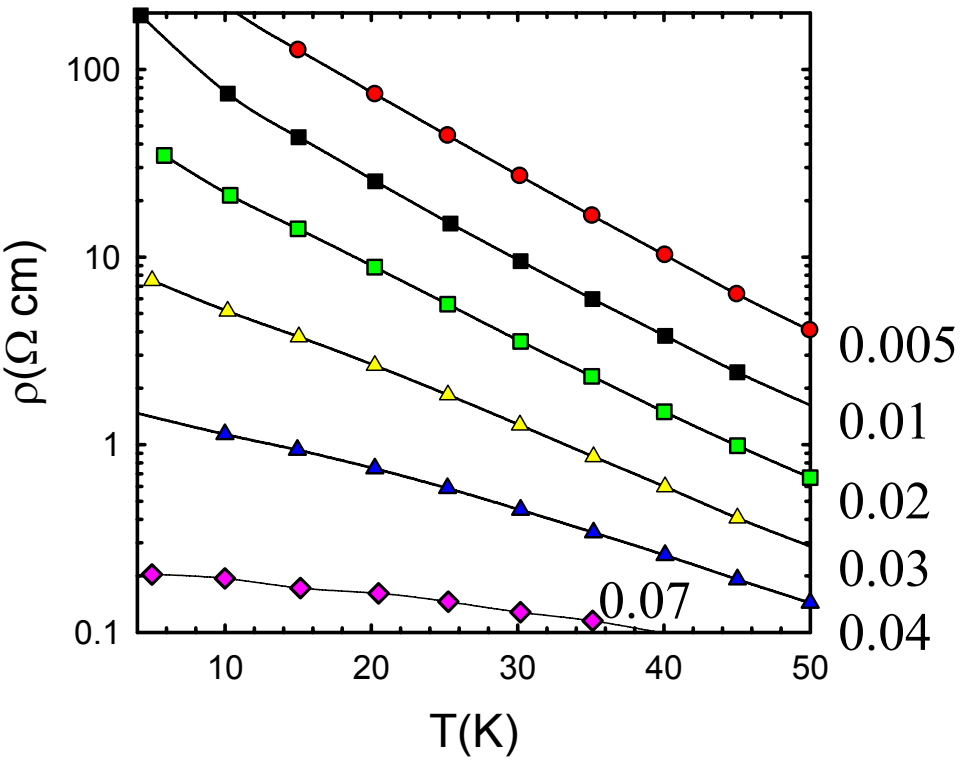

Fig. 4.4 *Low temperature resistivity versus temperature*

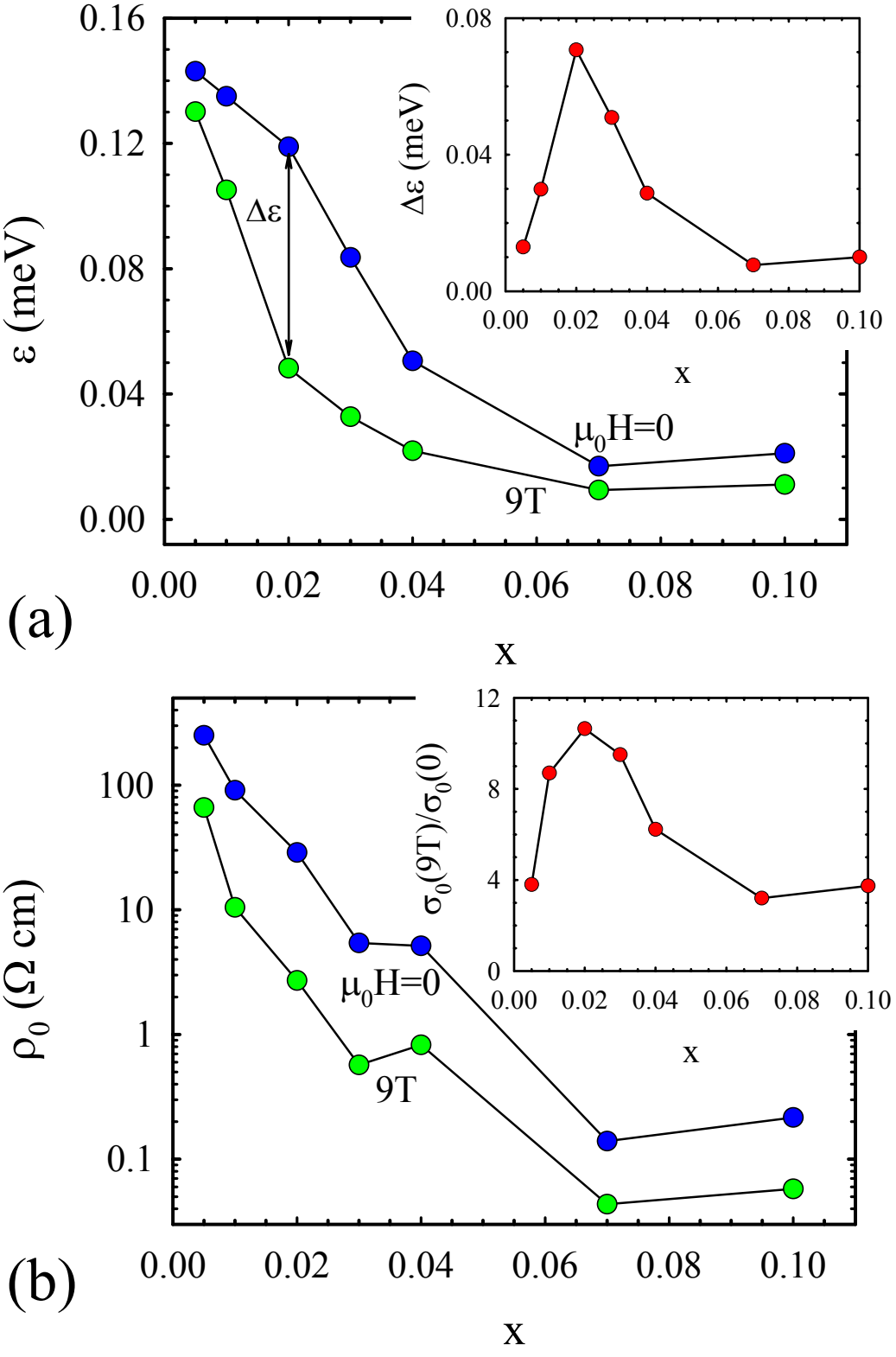

Fig. 4.5 *Low T activation energy and prefactor ρ_0 versus doping*

their 0-field resistivity shows an activated behavior (*Fig. 4.4*):

$$\rho = \rho_0 \exp\left(\frac{\varepsilon}{k_B T}\right)$$

Our measurements, done in fields of up to 9 T (much higher than those reported in *Ref. [12]*), reveal a significant decrease of both the activation energy ε and prefactor ρ_0 in the presence of the magnetic field (*Fig. 4.5*). The insets show plots of $\Delta\varepsilon = \varepsilon(0) - \varepsilon(9T)$ and $\sigma_0(9T)/\sigma_0(0) = \rho_0(0)/\rho_0(9T)$ which exhibit maxima at x=0.02.

Below the antiferromagnetic ordering temperature T_N~110-125 K, the normalized magnetoresistance $\Delta\rho/\rho = [\rho(H) - \rho(0)]/\rho(0)$ exhibits an increase by almost two orders of magnitude for the highest applied fields, going from ~0.01 in the paramagnetic phase to ~1 at T=4.2 K. Its behavior is shown in *Fig. 4.6*: for the lowest concentrations, x=0.005 and x=0.01 it has a quadratic magnetic field dependence in the lower field range. As the magnetic field increases, this dependence changes to approximately cubic.

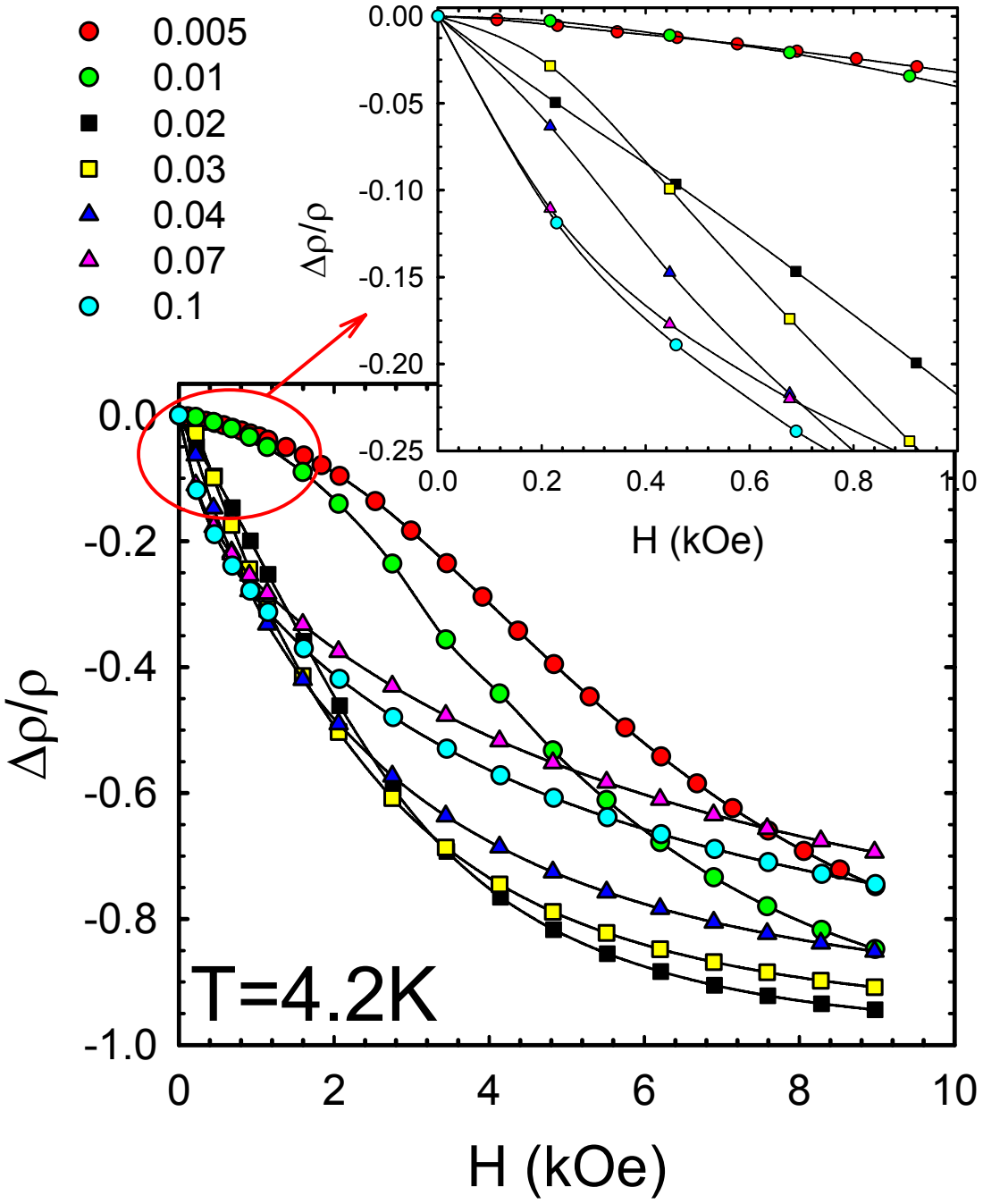

Fig. 4.6 *Magnetoresistance versus applied field at 4.2 K*

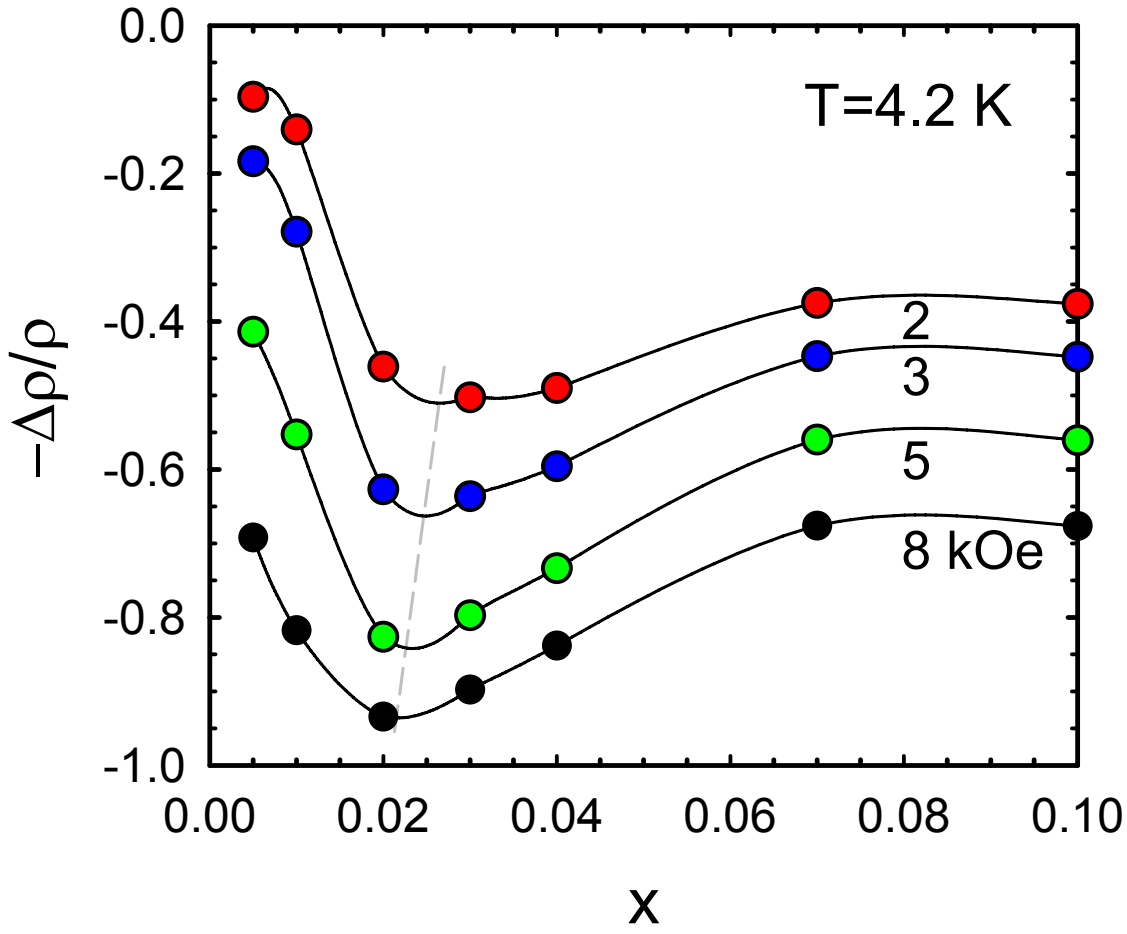

Fig. 4.7 *Magnetoresistance versus x for several values of the applied field*

The behavior of the magnetoresistance changes radically for the more heavily doped samples: x=0.07 and x=0.1. The change in magnetoresistance is much more abrupt at lower fields, but after this initial sharp decrease, its variation begins to saturate and at the higher fields the effect becomes smaller in magnitude than the one seen in lightly doped compositions. When plotted against La content x for several values of B, the magnetoresistance shows a maximum at x~0.02 for the higher fields (*Fig. 4.7*).

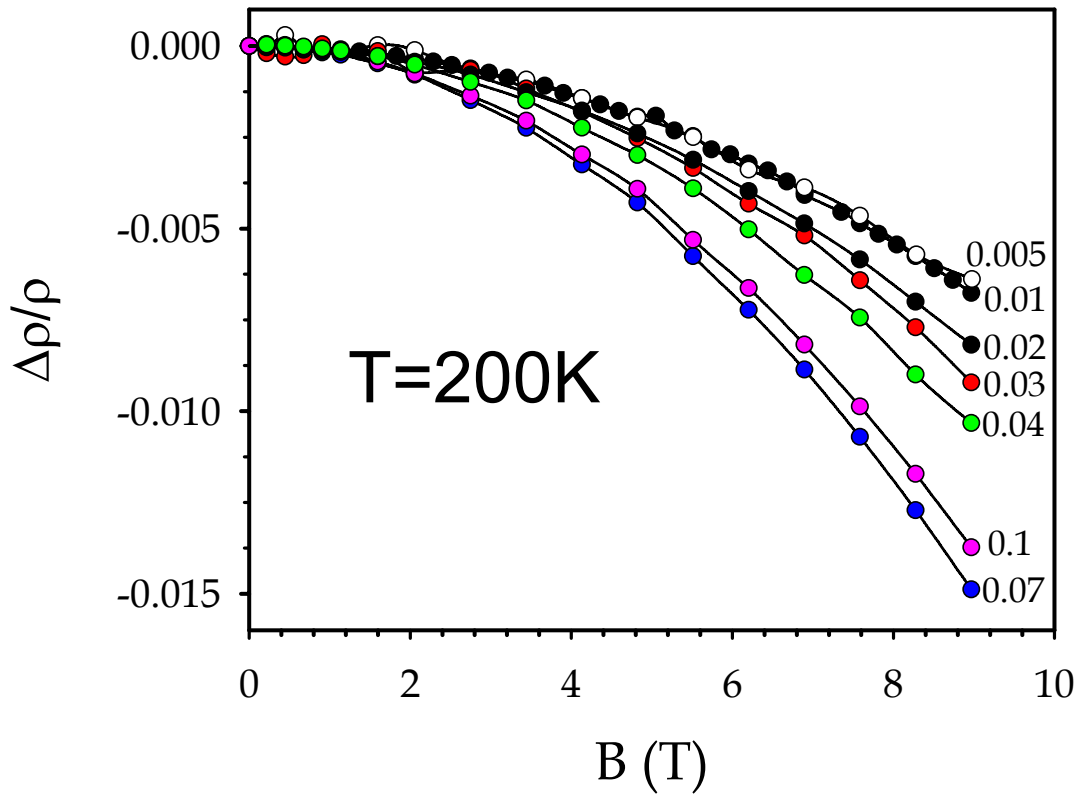

Fig. 4.8 *Magnetoresistance versus field in the paramagnetic phase*

4.2.3 Paramagnetic Phase

The quadratic field dependence of the magnetoresistance in the paramagnetic phase (shown in *Fig. 4.8* for *T*=200 K) resembles the behavior observed in the "colossal magnetoresistance" hole-doped counterparts, where a dependence of the form $\Delta\rho/\rho = -C[M(H,T)/M_S]^2$ is found to describe the data well near the Curie temperature[25]. An analysis along these lines (shown in *Fig. 4.9 a)* for five different temperatures) provides a good description of our data above the Nèel transition. An outstanding feature of this graph is revealed when calculating the parameter *C* (the slope

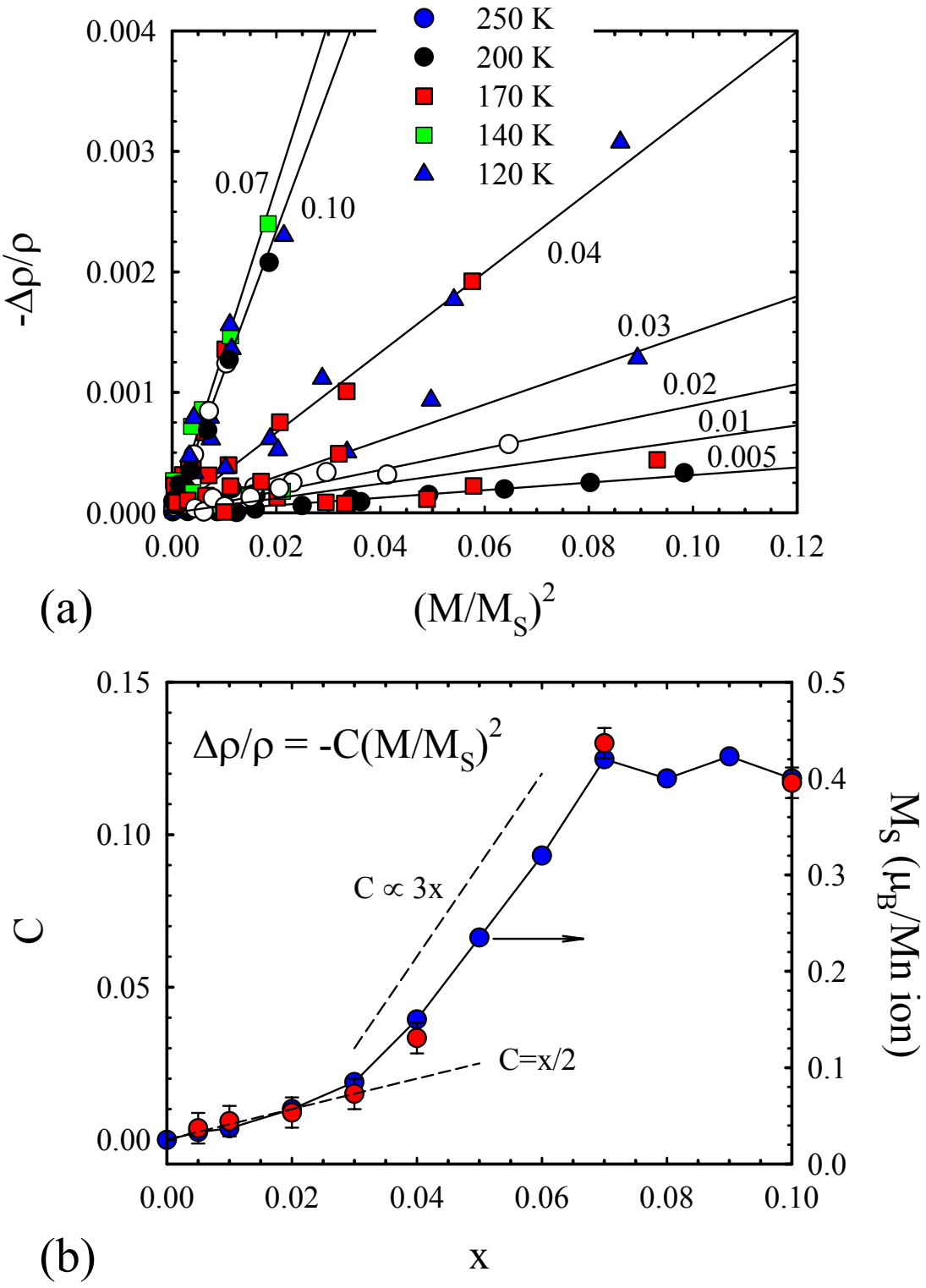

Fig. 4.9 *Magnetoresistance versus $(M/M_S)^2$ in PM phase (a) coefficient C versus x (b)*

of each curve) and plotting these values against x: C, follows the x-dependence of the saturation magnetization (*Fig. 4.1*) remarkably well, showing the same change in slope near x=0.02, changing from $C(x)=x/2$ for lightly doped compounds to $C(x)=3x$ as doping increases above 0.02.

4.3 Discussion

The presence of ferromagnetic domains (of approximate diameter of ~10 Å and separated by ~40 Å) embedded in the antiferromagnetic matrix of the parent compound is evidenced by the small angle neutron scattering (SANS) study of Granado *et al.*[14] but they find that the density of these droplets is ~60 times smaller than the electron concentration in these compounds. If these droplets are actually seven-site magnetic polarons formed by a Mn^{3+} ion spin aligned with its nearest neighbor Mn^{4+} spins (structures predicted to be the stable magnetic polaron state for this system[26,27]), then the majority of dopant electrons reside outside these droplets and understanding their spin configuration is crucial in order to explain $Ca_{1-x}La_xMnO_3$'s properties.

Both magnetization and resistivity measurements indicate that the "missing" electrons outside the droplets are important in modifying the antiferromagnetic background. The slope of the saturation magnetization versus x plot (*Fig. 4.1*) for $x \leq 0.02$ is approximately $dM_S/dx = 1\ \mu_B/Mn\ ion$, much smaller than one would expect for a picture in which each electron creates a seven site magnetic polaron. The low temperature resistivity decreases by five orders of magnitude for an increase in doping from 0 to 0.005 (*Fig. 4.10*). In this very light doping regime, the isolated droplets (separated by 40

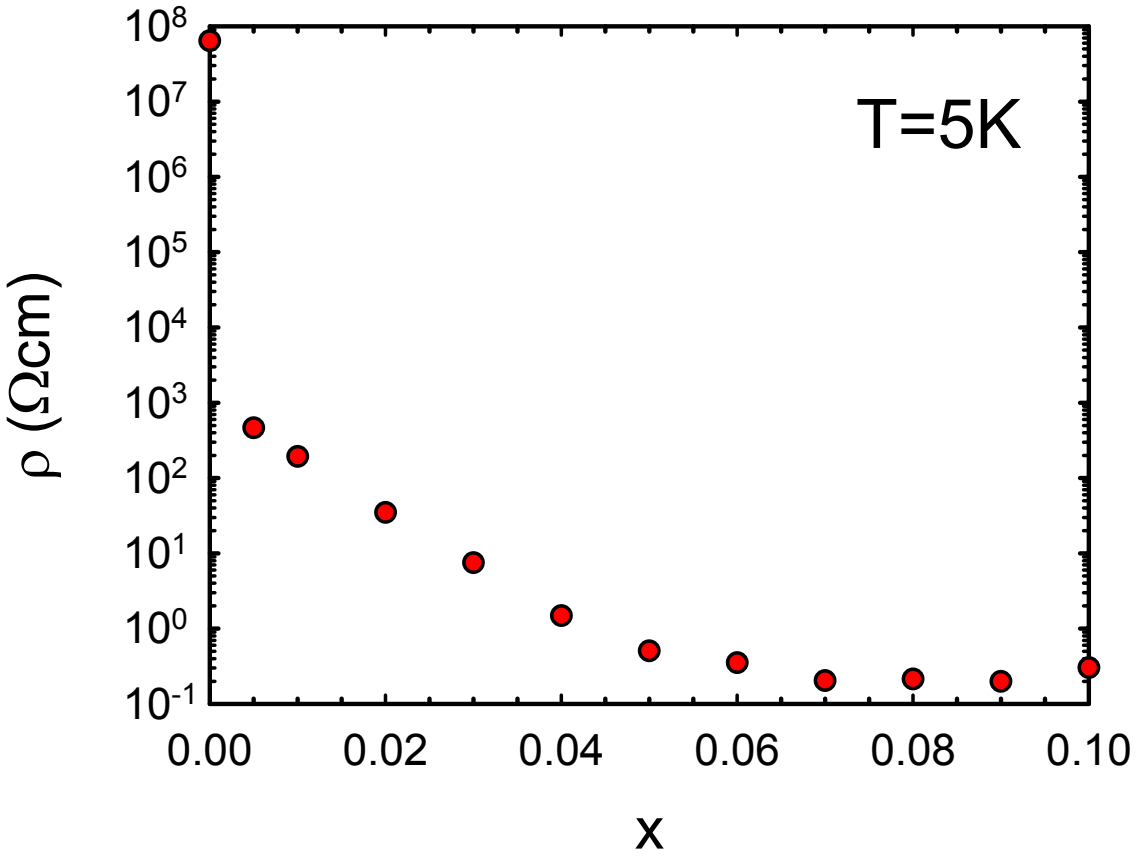

Fig. 4.10 *Resistivity versus doping for different $Ca_{1-x}La_xMnO_3$ compositions at T=5K*

Å or more) cannot dramatically improve the electron transfer to account for such a huge change in resistivity. The large magnetoresistance effect for $x \leq 0.02$ (non-interacting droplets regime) also argues against a scenario in which the ferromagnetic domains exist within the unaltered antiferromagnetic background of the parent compound.

It has been postulated that the missing electrons reside in spin canted regions outside the ferromagnetic droplets in the lower *x* regime, structures that are not identifiable by SANS studies. The existence of non-percolating spin canted regions at low doping might be capable of explaining magnetization, transport and neutron

scattering results[13] which show the development of a long range spin canted state for $x \geq 0.06$. Although the particular spin structure outside the droplets has yet to be determined, a plausible candidate has a ferromagnetic droplet surrounded by a spin canted region, structure which might naturally account for liquid like correlations in the distribution of the droplets observed in neutron scattering.

The changes in the doping and magnetic field dependencies of the susceptibility that occur near x=0.02 imply either an increase of spin canted cluster size or canting angle. At this concentration, the average distance between dopants $d = (4\pi n)^{-1/3} = 8.4\,\text{Å}$ is roughly twice the Mn ion separation or just the point when the overlap of seven-site magnetic polarons would be expected. But this seems to be just a coincidence since, as stated above, the slope of the magnetization in the low doping regime is a lot smaller than what it should be if each of the dopants creates an isolated polaron. The slope of the magnetization approaches the isolated polarons value for the higher dopings, but in this doping range there is already a long range spin canting. Thus, the correct picture is obviously more complicated.

The magnetoresistance in the ferromagnetic CMR manganites is quite well described empirically by $\Delta\rho/\rho = -C[M(H,T)/M_S]^2$ for $M/M_S \leq 0.3$. Various models have been proposed in order to explain the M^2 dependence: some of them are based on double exchange, other claim a magnetization dependent variable range hoping. Magnetic scattering due to ferromagnetic fluctuations is another possible scenario in the case of magnetic semiconductors and metallic ferromagnets. The lightly electron doped manganites behave in the paramagnetic phase more like heavily doped semiconductors[24]. As stated previously, in this temperature range the Hall coefficient is constant (implying a

constant carrier density) but there is a temperature dependence of the mobility. Thus, a magnetization dependent mobility seems to be a more suitable description of this system, with ferromagnetic fluctuations in the paramagnetic phase that tend to reduce ρ by providing double exchange pathways. Regardless of the model employed to explain the behavior of the magnetoresistance, it is useful to examine the magnitude and doping dependence of C relative to those of CMR compounds.

The magnitude of C is quite small relative to the "colossal magnetoresistance" compounds (for which C~1-7) but this is to be expected since the fraction of $Mn^{3+}O^{2-}Mn^{4+}$ (for which the ferromagnetic double exchange occurs) is only $2x$ and the $Mn^{4+}O^{2-}Mn^{4+}$ superexchange interactions dominate the magnetic fluctuations. Assuming that only the fluctuation contribution to the conduction is field dependent, the magnetoresistance and the magnitude of C should be proportional to the number of double exchange active bonds ($2x$). Thus our value of C=0.13 at x=0.07 for example is roughly equivalent to a value of $C/2x$~1 for a pure double exchange system.

Compelling evidence that the paramagnetic phase magnetoresistance is associated with ferromagnetic fluctuations is provided by the fact that $C(x) \propto M_S(x)$. Since the same crossover observed near x=0.02 in the magnetically ordered phase occurs above T_N as well, we conclude that these fluctuations have the same inhomogeneous structure present in the ground state: fluctuating ferromagnetic droplets and/or spin canted clusters begin to develop well above the ordering temperature.

Chapter 5

Polaron Transport in the Paramagnetic Phase of $Ca_{1-x}La_xMnO_3$

5.1 Prior Studies

Our study of lightly La doped manganese oxides continues with a closer look at the transport properties in their paramagnetic phase, where the behavior exhibited by the "colossal magnetoresistance" hole-doped counterparts is small polaronic[29].

Although we examine the lightly electron doped regime (i.e. the concentration of dopants remains far below the threshold for which overlap effects occur) in which the antiferromagnetic superexchange is dominant, the effects of double exchange and Jahn-Teller coupling to the lattice remain important. In this doping range, a weak ferromagnetic moment associated with an intrinsically inhomogeneous ground state develops with increased doping level[30].

Previous transport studies in the paramagnetic phase of electron-doped manganites[12,31-33] show that their properties differ substantially from those of the CMR compositions. The thermally activated behavior exhibited by both the resistivity and thermopower of CMR compounds is replaced by a positive temperature coefficient of resistivity at high-T and a thermopower that decreases with decreasing temperature.

The present work focuses on charge carrier transport around and above the transition temperature of $Ca_{1-x}La_xMnO_3$ with the purpose of explaining the role and nature of polarons in the paramagnetic phase of electron doped compounds. It will be shown that the magnitude of the Hall mobility and its temperature dependence do not favor a small polaron picture, successful in describing the paramagnetic phase of the hole doped compounds. The analysis of both the mobility and thermopower using a large polaron model implies an intermediate coupling regime with a phonon coupling constant α~5.4, an electron effective mass m^*~4.3m_0 and a polaron mass m_p~10m_0.

5.2 Results

Fig. 5.1 shows the resistivity versus temperature for all the studied specimens. From a qualitative point of view, the resistivity decreases with increased doping and shows a positive temperature coefficient for T≥200 K as previously reported in similar electron doped manganites[12-14,33].

In *Fig. 5.2* the Hall voltage is plotted versus magnetic field for several compositions. Two characteristics of these plots need to be mentioned: the linearity in field and the fact the $V_H<0$ (electron-like). The Hall coefficient is given by the slopes of these curves:

$$R_H = \frac{dV_H}{d\left(\mu_0 H\right)}\frac{t}{I}$$

where t is the thickness of the sample and I is the current. The Hall number is then calculated using $n_H = V_{f.u.}/R_H|e|$ and it should be equal with the number of carriers per

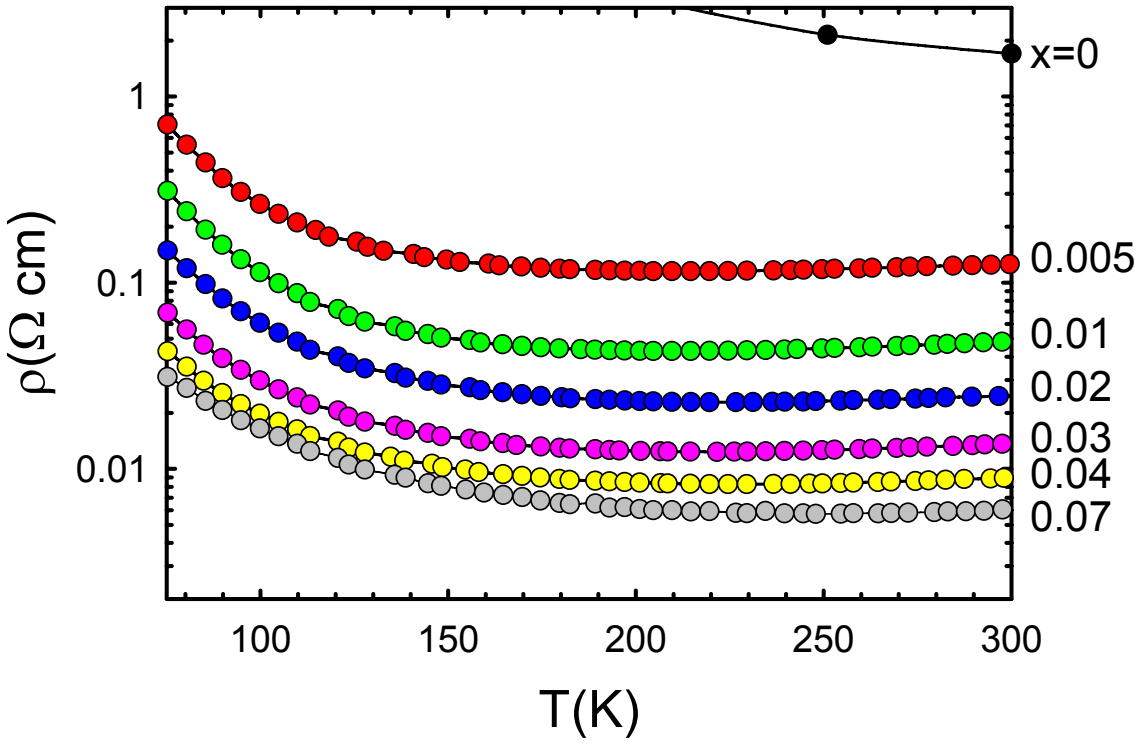

Fig. 5.1 *Resistivity versus temperature for* $Ca_{1-x}La_xMnO_3$

formula unit (shown in *Fig. 5.2 (b)* as a function of doping for T=250 K with $V_{f.u.}$=205/4 Å[13,14]). Although $V_{f.u.}$ varies slightly throughout the x range, these variations are much smaller than the experiment accuracy and were neglected. The fact that n_H=-x confirms that doping adds x electrons per formula unit.

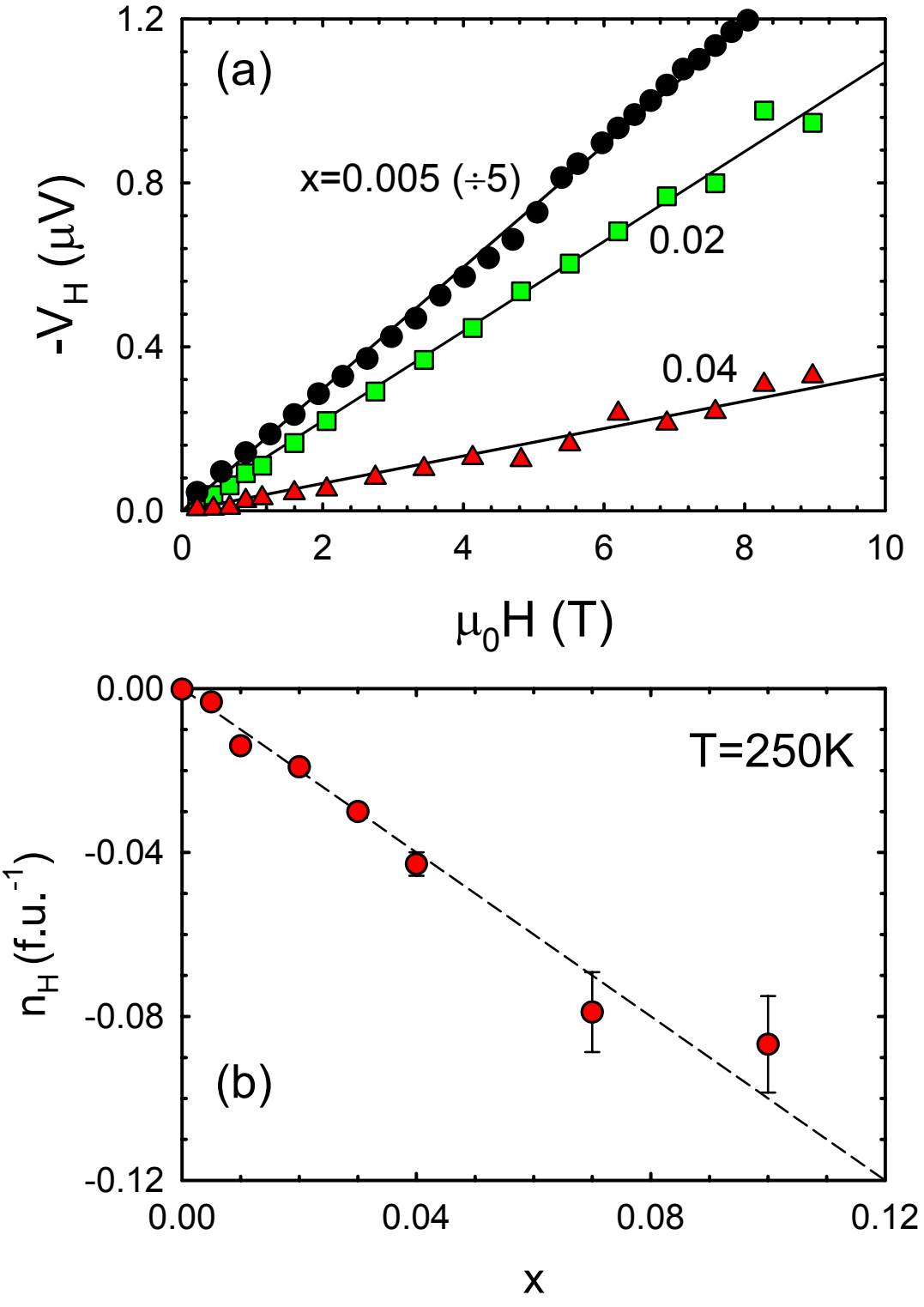

Fig. 5.2 *a) Hall voltage versus magnetic field and b) Hall number versus x*

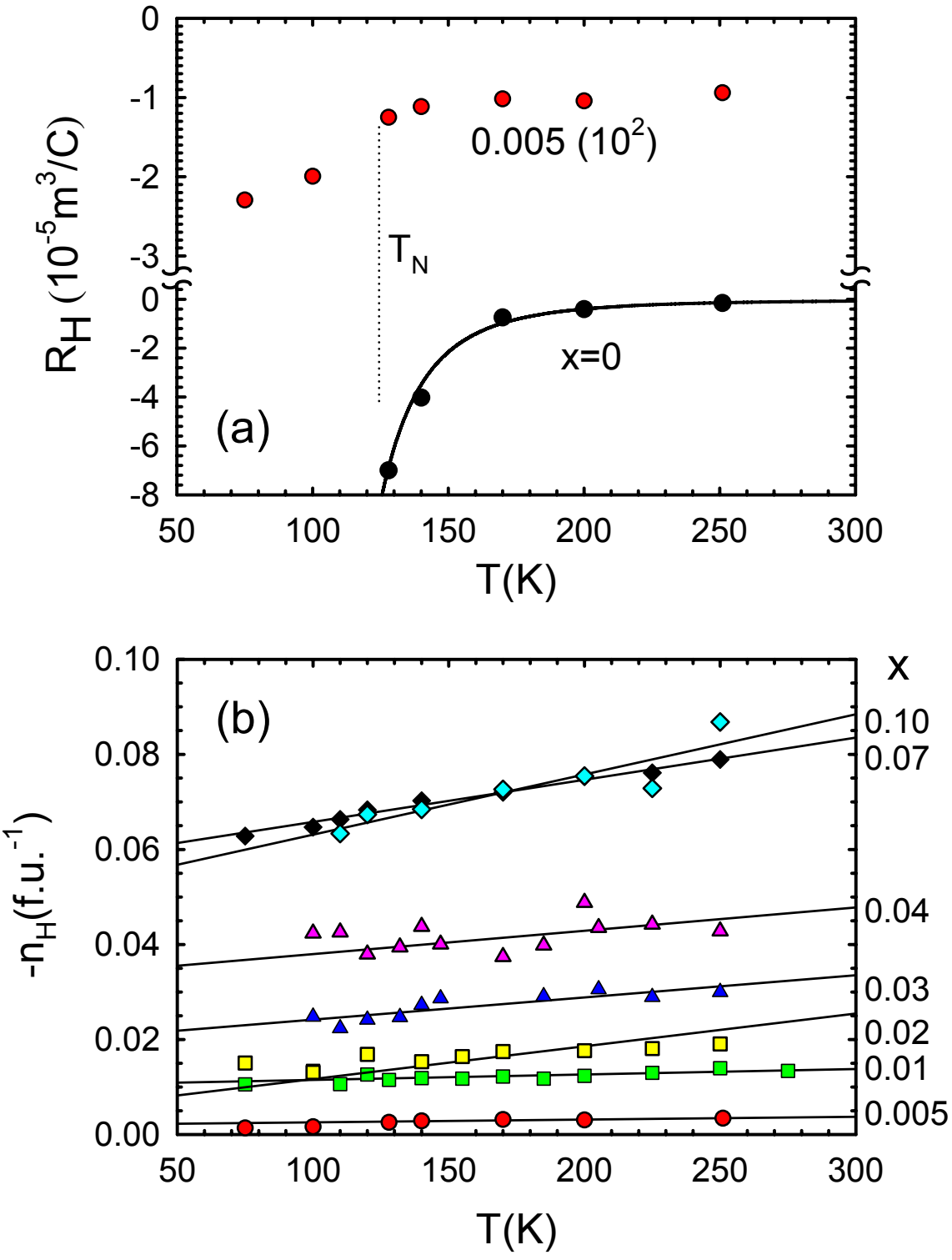

Fig. 5.3 *a) R_H versus T for x=0, 0.005 b) n_H(T) for x>0.005*

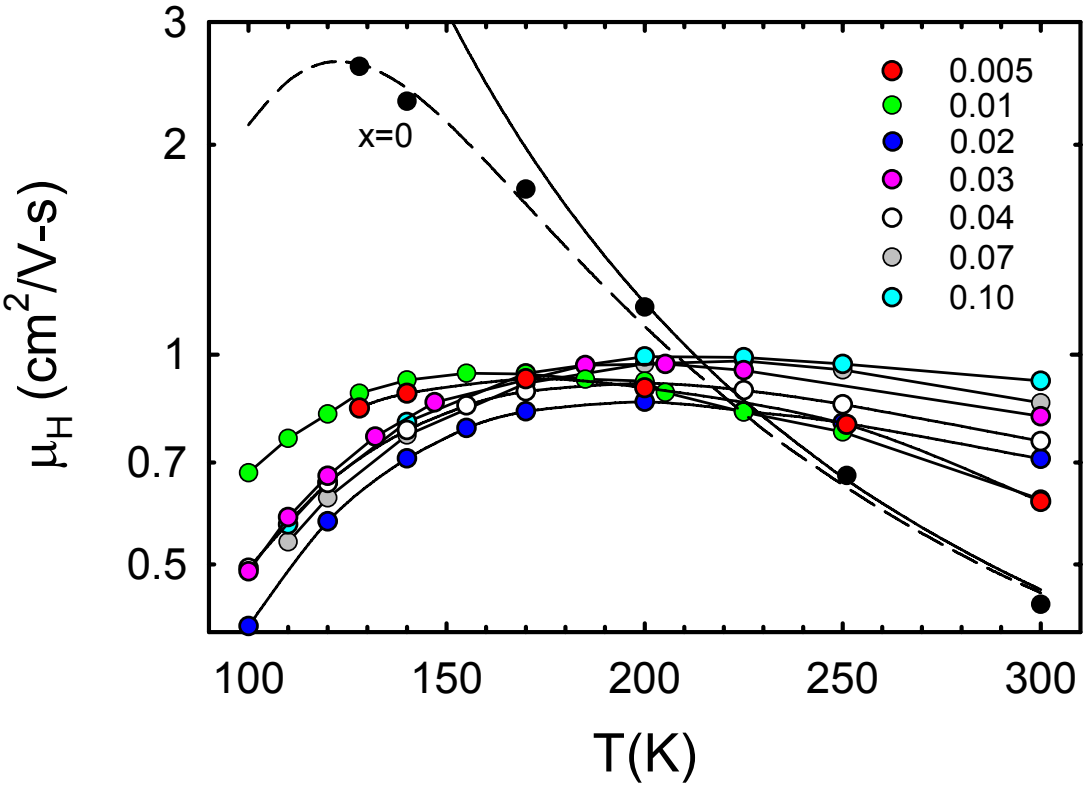

Fig. 5.4 *Hall mobility versus temperature for all polycrystalline specimens*

The dependence of $R_H(T)$ in the PM phase is shown in *Fig. 5.3 (a)*: simple activated behavior for CMO of the form n_H=-1.25x10^{-2}*exp*(-1010/*T*).

The Hall mobilities, calculated using $\mu_H \equiv R_H / \rho$ and linear least square fits of the n_H versus T data and plotted in *Fig. 5.4* for all compositions, show a behavior qualitatively similar to that of polar semiconductors. For the CMO specimen, the mobility increases strongly with decreasing temperature from a room temperature value of μ_H=0.5 cm^2/Vs, in contrast with the much more gradual increase with maxima around 150~200 K shown by the doped samples.

If we compare the room temperature magnitude of the mobility of the single crystal (CMO) relative to the polycrystalline doped samples, it is intriguing to observe that μ_H is actually smaller in the former. Our $CaMnO_3$ single crystal had a carrier density between that of the x=0 and x=0.005 polycrystals and a resistivity slightly larger than that of the polycrystalline x=0 sample, and thus implying a lower value of μ_H for the crystal. In general, additional scattering centers, in this case provided by the grain boundary, tend to increase the resistivity without a sizable effect on R_H even for highly anisotropic materials[34]. Thus we conclude that grain boundary scattering has minimal effects in determining the behavior of the Hall mobility.

Another thing to be noted is that both the magnitude and the overall T dependence of μ_H for the present compounds contrasts with those observed for the hole doped compounds. μ_H for the electron doped compounds is nearly two orders of magnitude larger, while the activated behavior of the mobility for the CMR compounds contrasts with the one observed here. When plotted versus Hall carrier density at fixed temperature, μ_H shows a weak, systematic increase (*Fig. 5.5*).

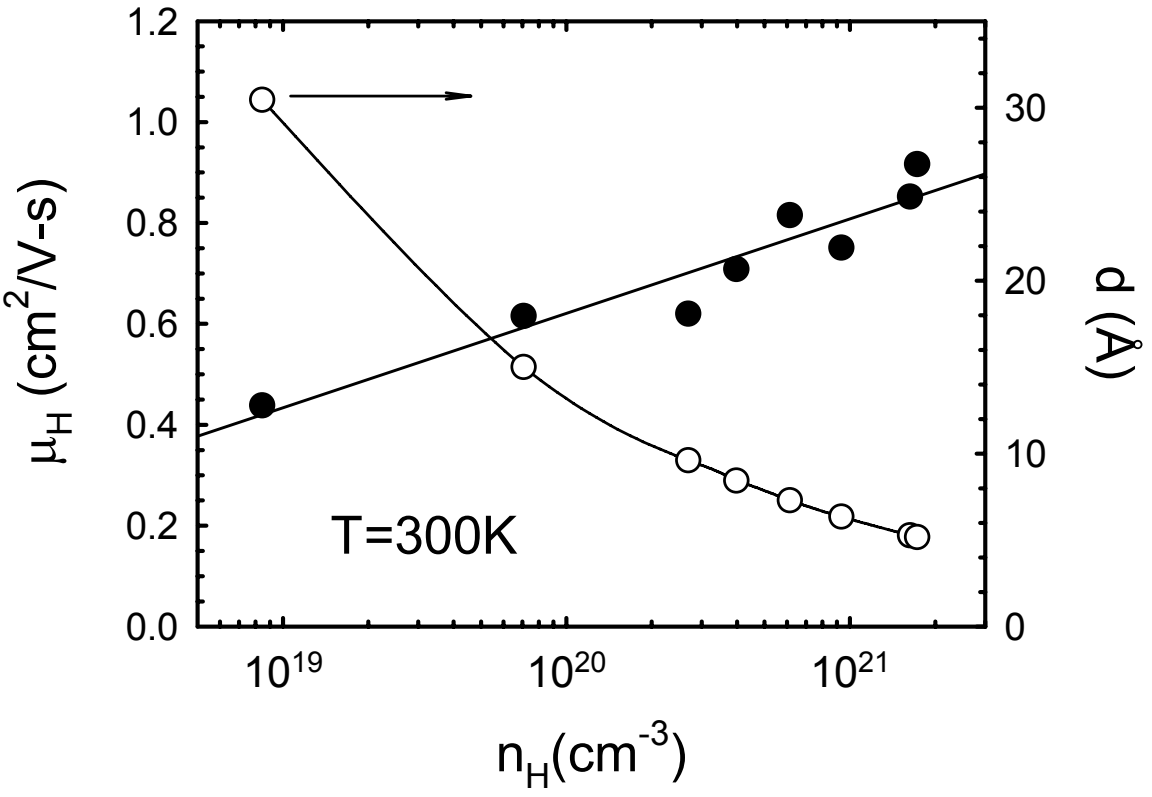

Fig. 5.5 *Hall mobility and mean dopant spacing versus Hall carrier density at room temperature*

Like the Hall mobility, the thermoelectric power data (shown in *Fig. 5.6*) exhibits different behavior for various doping levels. The TEP for CMO increases with decreasing temperature from a room temperature value of ~ -550 μV/K. This behavior is consistent with an activated form similar to the one seen in the resistivity and Hall carrier density data. Thermopower's behavior changes with increasing doping level, moving away from the thermally activated behavior observed in CMO and also in the PM phase of the CMR compounds and becomes similar to the TEP for a degenerately doped semiconductor[35] (and similar to that of Sm and Pr doped CMO[31,32]).

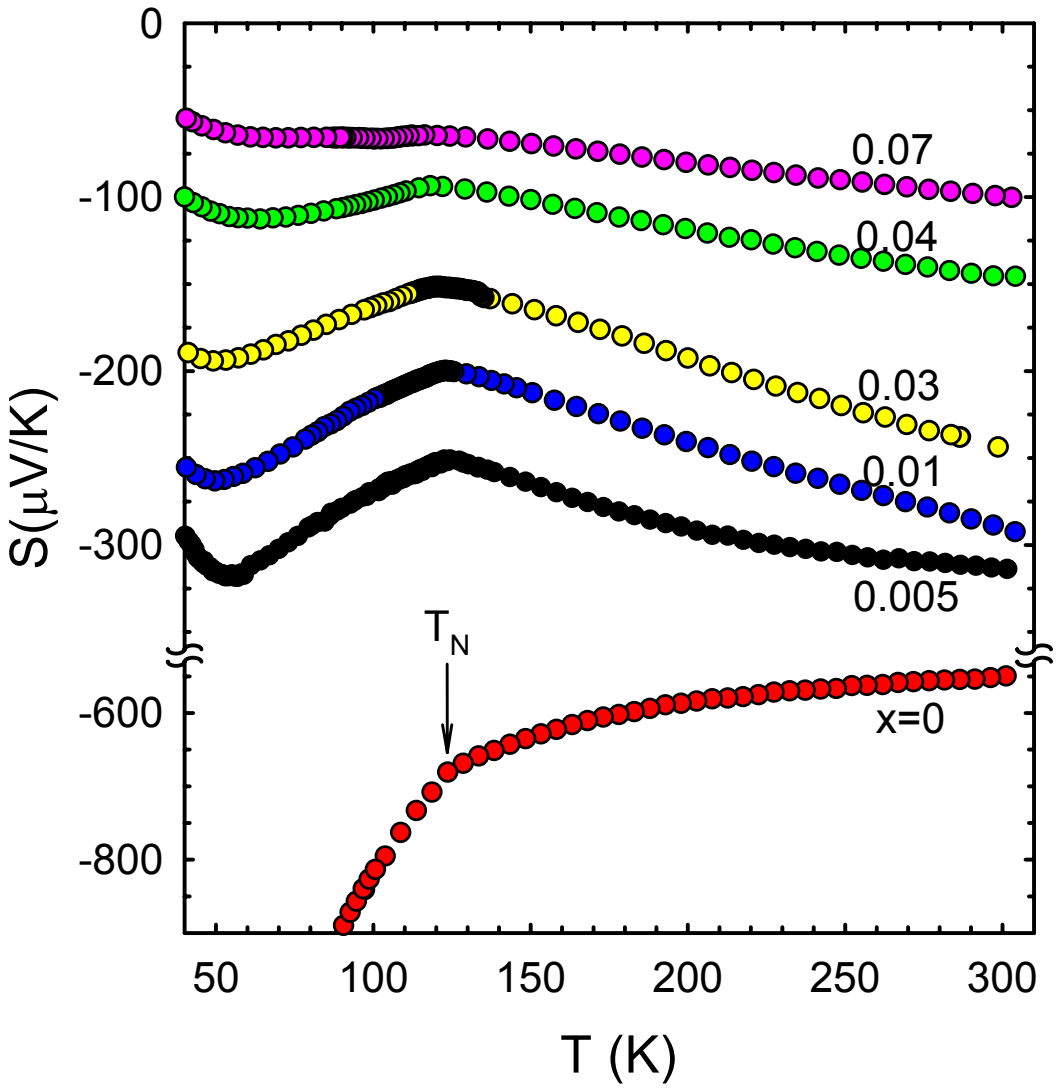

Fig. 5.6 *Thermoelectric power versus temperature*

For all specimens, the thermoelectric power decreases abruptly with the transition to the antiferromagnetic phase. This is to be attributed to a decrease in double exchange electron transfer as a result of the antiferromagnetic ordering of Mn spins which enhances the TEP magnitude. This reduction in the carrier concentration and/or mobility below T_N is consistent with our previous observations regarding the Hall coefficient.

5.3 Analysis and Discussion

The magnitude and temperature dependence of the Hall mobility and thermopower are incompatible with the small polaron theory. Dielectric constant studies[36] show a static dielectric constant ε_0=40 in $CaMnO_3$, substantially larger than the optical value reported for manganites[37], $\varepsilon_\infty = 5$. These observations motivate a Fröhlich (i.e. large) polaron description for the charge carriers in this system.

The dimensionless polaron coupling constant is givene by[38]:

$$\alpha = 397.4\left[\frac{\left(m^*/m_0\right)}{\Theta}\right]^{1/2}\left(\varepsilon_\infty^{-1} - \varepsilon_0^{-1}\right),$$

where m^* is the band mass (without polaron enhancement), m_0 is the free electron mass, $\Theta = \hbar\omega_0/k_B$ and ω_0 the longitudinal optical phonon frequency. If we take the longitudinal optic phonon energy[51] Θ=700 K, $m^*=m_0$ then α=2.6. The donor binding energy and dielectric constant[36] of CMO suggest $m^*\sim 4m_0$, so a proper treatment of the transport properties requires a theory more suitable for an intermediate coupling regime: $2 \le \alpha \le 6$.

The most reliable theory for large polaron mobility at intermediate coupling and intermediate temperature is that of Feynman *et al*.[39] The polaron mobility is given (cm^2/Vs) by:

$$\mu_p = \frac{7.14\times10^4}{\alpha\Theta}\left(\frac{m_0}{m^*}\right)\frac{\sinh\left(z/2\right)}{\left(z/2\right)^{5/2}}\frac{w^3}{v^3}\frac{1}{K\left(v,w,z\right)}$$

where z=Θ/T. The integral $K(v,w,z)$ and the procedure for determining the variational parameters *v* and *w* at each temperature for a given value of m^*/m_0 are described in detail in literature[40]. An analysis similar to the one above with m^*/m_0=4.3 and Θ=700 K gives us the solid curve in *Fig. 5.4*. The discrepancy between experiment and the fitting curve is attributable to an increasing influence of impurity scattering. An additional term was added to correct for that (Brooks-Herring mobility)[41]:

$$\mu_{BH} = \frac{3.68\times10^{-3}}{N_1}\frac{1}{Z^2}\left(\frac{\varepsilon_0}{16}\right)^2\left(\frac{T}{100}\right)^{3/2}\left(\frac{m_0}{m^*}\right)^{1/2} f(\beta),$$

$$f(\beta) = \left[\ln\left(1+\beta^2\right) - \frac{0.434\beta^2}{1+\beta^2}\right]^{-1},$$

$$\beta = \left(\frac{\varepsilon_0}{16}\right)^{1/2}\left(\frac{T}{100}\right)\left(\frac{m^*}{m_0}\right)^{1/2}\left(\frac{2.08\times10^{18}}{n}\right)^{1/2}$$

The dashed curve through x=0 mobility represents $\mu = \left(\mu_p^{-1} + \mu_{BH}^{-1}\right)^{-1}$ using $n=n_H$, Z=2, ε_0=40 and m^*/m_0=4.3. The only free parameter left, the impurity concentration, was found to be 3x10^{19} cm^{-3}, roughly four times larger than T=300K Hall carrier concentration. The disagreement is reasonable when considering that in the Brooks-Herring term only the charge carrier concentration is taken into account but not the lattice distortions: long range correlated disorder that appears due to corner sharing Mn-O octahedra.

The Feynman path integral theory gives a polaron mass at room temperature of $m_p = (v/w)^2 m_0 = 36m_0$ (larger than other models) and a radius $R_p = \left(3\hbar/2\mu v\right)^{1/2} \approx 3$ Å. This value of R_p is consistent with the seven site magnetic polaron formation in CMO, predicted to be a stable ground state for this compound[26,27].

The simple sum of scattering terms that was used to fit the CMO data cannot be used for the doped specimens since it assumes isolated polarons, a condition that may not be appropriate for the doped specimens.

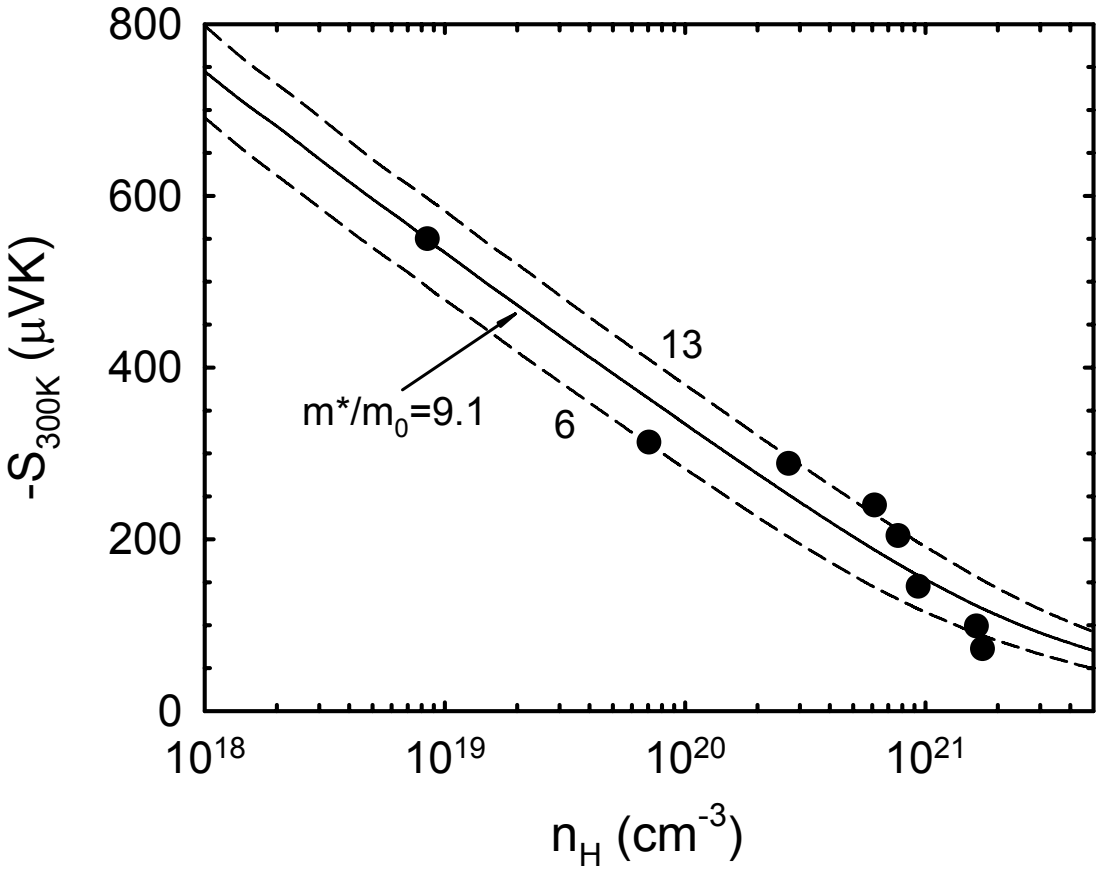

Fig. 5.7 *Room temperature thermoelectric power versus Hall carrier density*

A less reliable method of estimating the effective mass is offered by the thermoelectric power. The lack of theoretical work for the intermediate coupling regime makes the theory of Howarth and Sondheimer[42] the only one that can be used in an attempt to model the TEP. Their theory – not entirely suitable since it does not take into account impurity scattering - is a perturbative one in the weak coupling regime and, like

other weak coupling theories, they tend to overestimate the band effective mass. This theory fits the data well only at high temperatures and that is why our analysis is restricted to this range. As the temperature goes down, the growing role played by the impurity scattering and a temperature dependent polaron mass in these oxides makes it unfit to explain our data.

The HS theory gives TEP as a function of the phonon energy and reduced chemical potential. Again, for Θ=700 K and the chemical potential determined from Hall carrier density assuming a parabolic band, the thermopower can be computed with the effective mass m^{**} the only adjustable parameter. *Fig. 5.7* shows fits of the room temperature thermoelectric power for various m^{**}/m_0 ratios, with the best fit obtained for m^{**}/m_0=9.1. The mismatch between calculated and measured TEP magnitudes, corresponding to variations in m^{**}/m_0 from 6 to 13, could come from variations of the polaron mass with doping or from small variations in the oxygen vacancy concentration.

The electron doped manganese oxides are evidently near a crossover between large and small polaron behavior. The appropriate theoretical framework for studying these compounds remains an active area of investigation.

Chapter 6

Impurity Conduction in Antiferromagnetic Oxides

6.1 Polarons and Manganese Oxides

In a very general way, a polaron can be defined as a quasi-particle formed by a bound charge and the local polarization and distortion of the surrounding lattice (both created by the bound charge itself) that follows it and that may extend several atomic spacings away from it. A magnetic polaron is the result of the exchange interaction between an electron and the surrounding magnetic ions which leads to a localized (and magnetically polarized) perturbation of the magnetic lattice. Although these concepts were formulated long ago[43], the interest in polaron physics has been stimulated recently due to the key role they are believed to play in CMR materials and dilute magnetic semiconductor oxides (materials with localized spins and mobile carriers in interaction). The low electron concentration associated with oxygen deficiency in $CaMnO_3$ (*CMO*) and $SrMnO_3$ *(SMO)* makes them ideal systems for studying polaron physics due to their simplicity: Jahn-Teller active Mn^{3+} ions are largely absent and so are the complex collective interactions that characterize the more studied hole-doped counterparts.

The existence of seven-site magnetic polarons in the ground state of La-doped $CaMnO_3$ has been probed by means of magnetization, magnetotransport and neutron scattering measurements[12,14]. Whether they are formed solely due to magnetic exchange interactions of the electron with the surrounding magnetic ions (self-trapped magnetic

polarons) or by electrons trapped in Coulomb potentials which have the capability of polarizing surrounding spins (bound magnetic polarons) is still an open question since there is no reliable way to distinguish between the two.

The present study addresses the issue of bound versus self-trapped magnetic polarons and will show that a favorable electronic band structure, consisting of a band of mobile states at an energy δ above those of electrons bound in Coulomb potentials, could help make a distinction between the two. In the presence of very weak electric fields (F<50 V/cm) the bound electrons are promoted in this impurity band, leading to an increase in mobile carrier density by several orders of magnitude. Similar behavior is to be expected in other oxides, providing the means of studying highly correlated electron systems with a tunable mobile carrier density.

6.2 Results and Analysis

Although both CMO and SMO (orthorhombic and cubic respectively) are G-type antiferromagnets below a Nèel temperature T_N~125 K and 230 K respectively, a small ferromagnetic moment (0.02-0.03 μ_B/Mn ion) develops in both (*Fig. 6.1*): very gradual in SMO and at temperatures much smaller than T_N, but much more abrupt in CMO at $T \sim T_N$. While in SMO, this magnetic moment has been attributed to the formation of magnetic polarons[14], the lower CMO crystal symmetry allows for spin canting associated with Dzyaloshinsky-Moriya coupling[44,45]: antisymmetric exchange interaction that occurs in Anderson's superexchange model when spin-orbit coupling is taken into account.

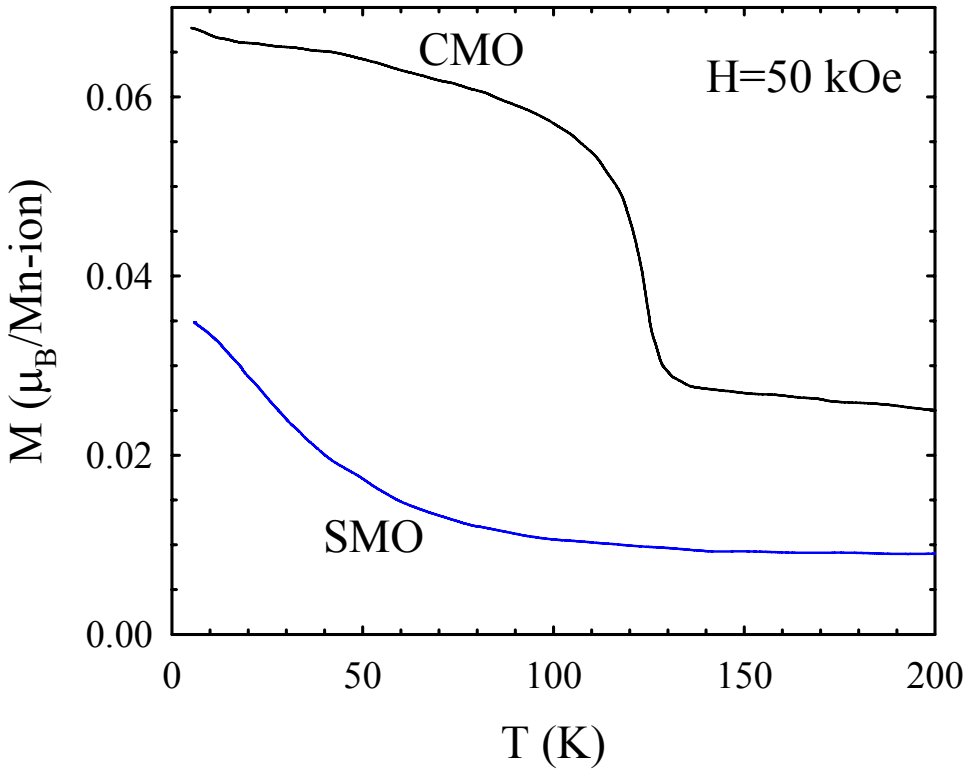

Fig. 6.1 *Magnetization versus temperature at 5T*

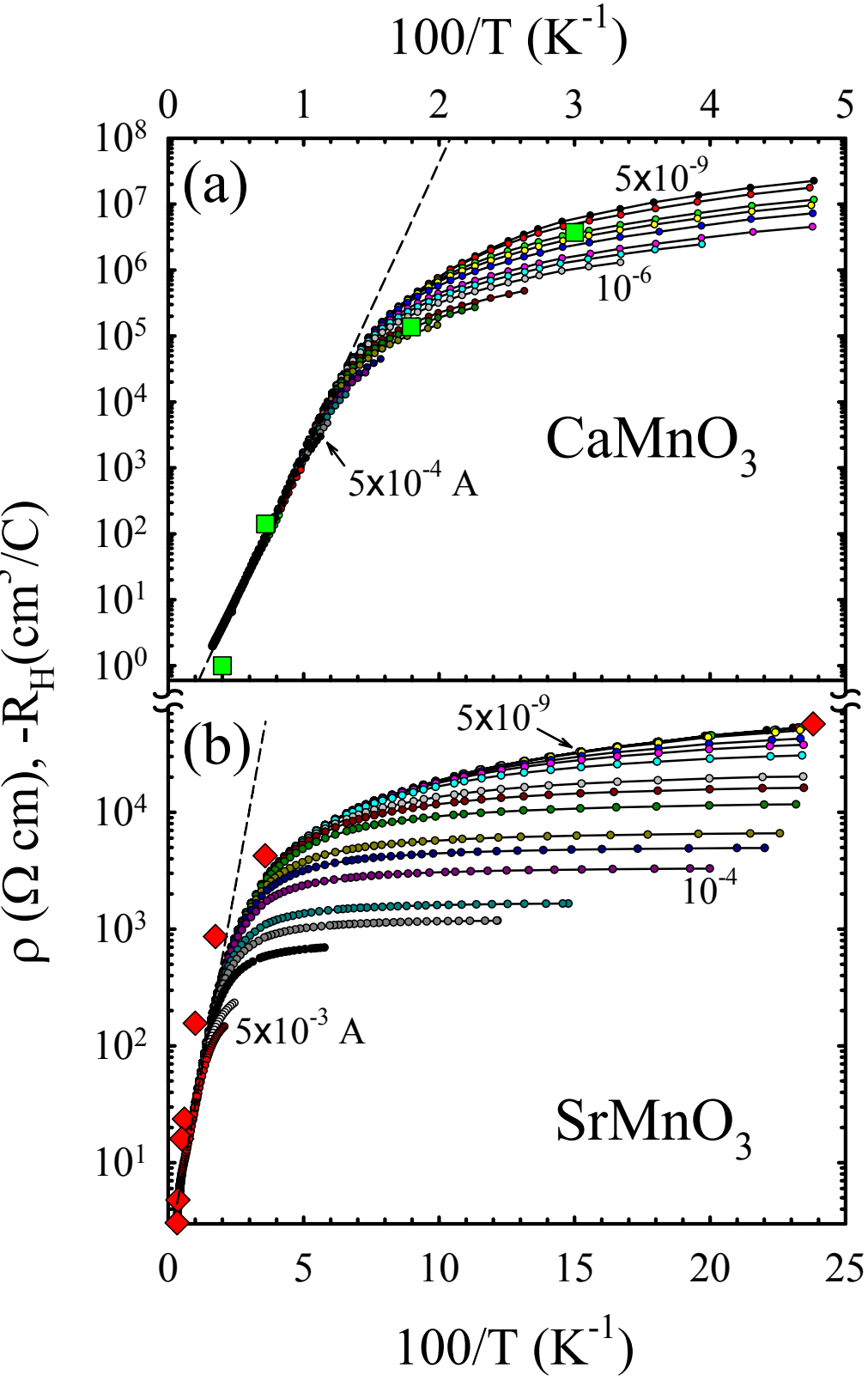

Fig. 6.2 *Resistivity and Hall number versus inverse temperature*

Fig. 6.2 shows a plot of DC resistivity against inverse temperature for various sample currents ranging from 5 nA to 10 mA (in steps of 1, 3, 5 per decade, several of which are labeled). At higher temperature, ρ for both *CMO* and *SMO* has simple activated form $\rho \propto \exp\left(\Delta / k_B T\right)$ with activation energies of Δ_{CMO}=86 meV and Δ_{SMO}=25 meV (dashed lines), both consistent with thermal activation of the electron into the conduction band. In the low temperature range ρ's behavior changes dramatically: it becomes extremely sensitive to transport current, decreasing by several orders of magnitude as the applied current increases. Throughout the whole temperature range, the resistivity's behavior is closely followed by that of the Hall coefficient R_H (green squares for CMO, red diamonds for SMO): activated behavior at higher temperatures followed by a weak temperature dependence in the low-T range consistent with a freeze-out of the carriers in donor levels, very few of them being mobile enough to contribute to R_H.

Fig. 6.3 (a) shows the variation of the conductivity σ (normalized to the value corresponding to the lowest current, σ_0) with the applied electric field $F=\rho J$ at fixed temperature. The scaling with the square root of the field $\sigma / \sigma_0 = \exp\left(-\alpha\sqrt{F}\right)$ is consistent with a Poole-Frenkel effect: a decrease in the height of a coulombic potential barrier under the influence of an external electric field (*Fig. 6.4*).

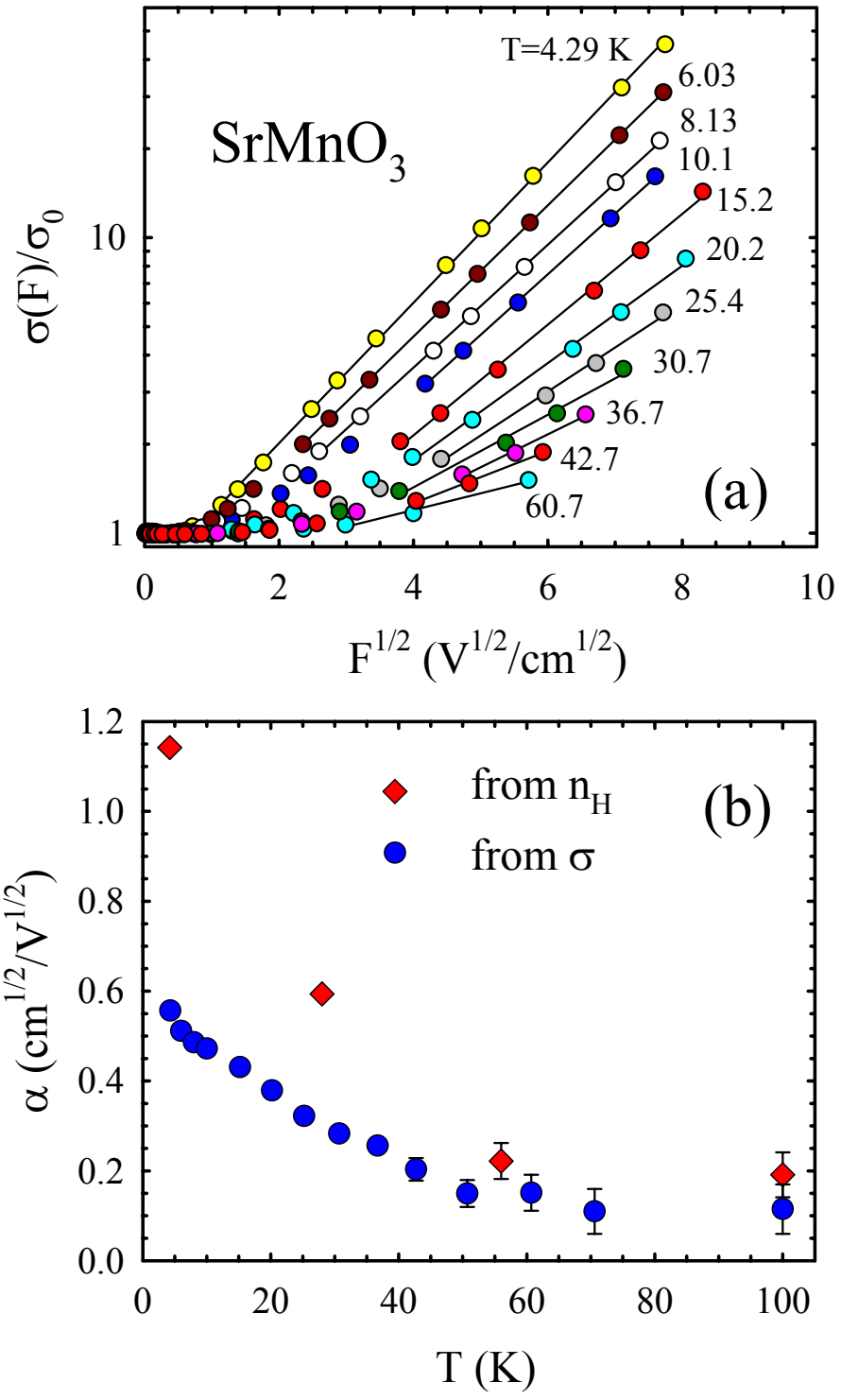

Fig. 6.3*Conductivity versus field (a) and coefficient α versus temperature*

The conductivity versus temperature curves (at fixed currents), which show some heating only for the maximum applied currents (limited to 2-3 K) were then interpolated for the same values of the temperature and cuts of these curves are shown in *Fig. 6.3 (a)*. Similar effects were observed in other manganese oxides: polycrystalline CMO, a nominally undoped polycrystal of $Ca_{0.25}Sr_{0.75}MnO_3$.

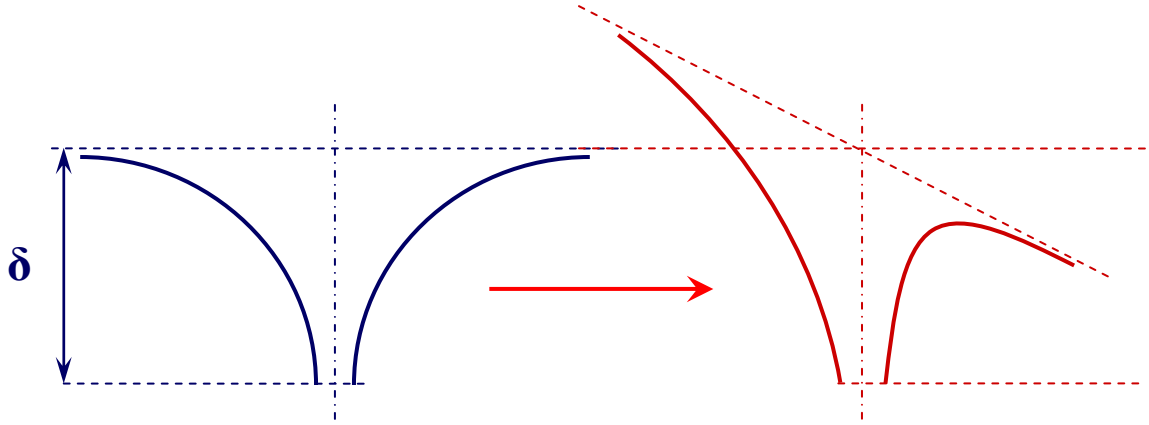

Fig. 6.4 *Poole-Frenkel field assisted ionization*

Fig. 6.3 (b) shows the dependence of the parameter α with the temperature determined from the slopes of the least-square fits of the conductivity curves in the non-Ohmic regime: α was found to be independent of an external magnetic field.

The current and magnetic field dependence of the Hall resistivity is shown in *Fig. 6.5*: ρ_{xy} increases to a maximum ($\mu_0 H$~3 T) and becomes linear in field above $\mu_0 H$~5 T. This type of behavior is characteristic of a sum of normal and anomalous Hall contributions (see *Fig. 3.8*). This is consistent with the magnetization versus field plot (inset *Fig. 6.5*), which shows the same type of behavior: a linear field dependence of both

magnetization and hall resistivity above ~5T which is consistent with the saturation of the anomalous (ferromagnetic) contribution.

The normal Hall coefficient was determined from high field slopes, $R_H = d\rho_{xy}/d(\mu_0 H)$. Both R_H and the anomalous contribution to Hall resistivity (intercepts of solid lines) decrease with increasing current consistent with an increase in

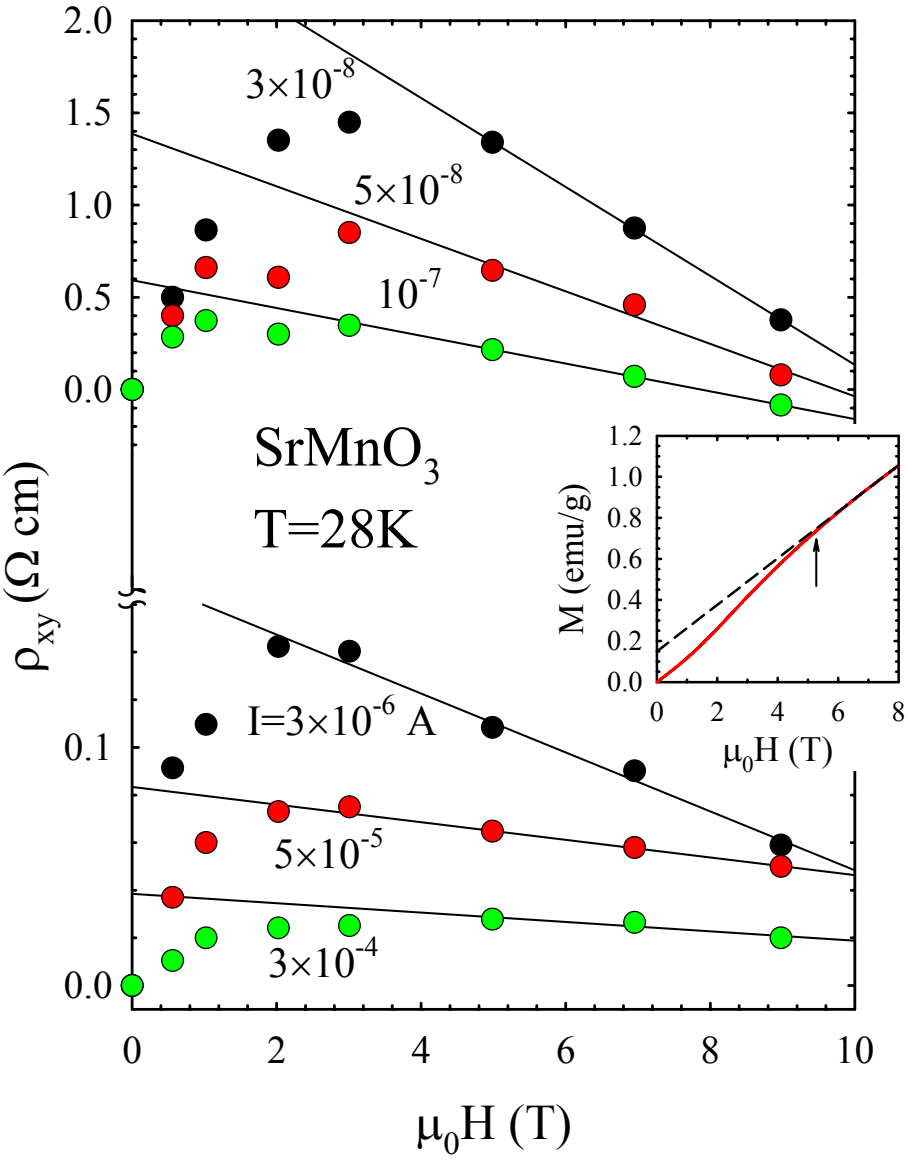

Fig. 6.5 *Hall resistivity and magnetization (inset) versus applied magnetic field*

mobile carrier density.

Fig. 6.6 shows the dependence of Hall carrier density versus transport field for CMO and SMO at several temperatures. The linear dependence of $\log(n_H)$ with $F^{1/2}$ is clear but a more formal description of the ionization rate in the Poole-Frenkel effect

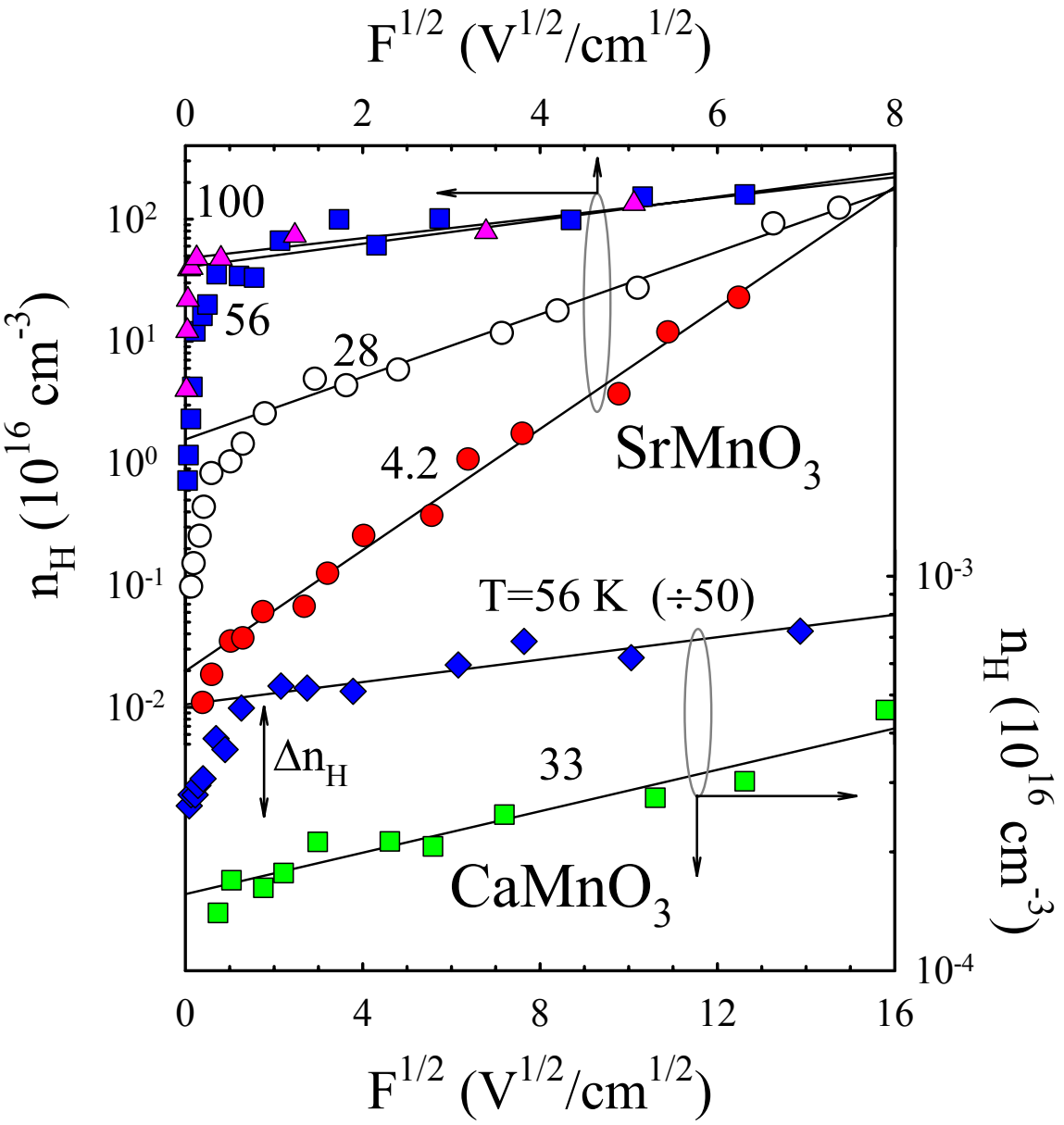

Fig. 6.6 *Hall carrier density versus* $F^{1/2}$

should include a thermal activation term besides the one describing the field induced ionization:

$$n_H(F) = N_0 \exp\left[-\left(\delta / k_B T - \alpha\sqrt{F}\right)\right]$$

The scale for barrier lowering, α, is set by $\alpha = \beta / k_B T$ where $\beta = \left(Ze^3 / \pi\varepsilon_0\varepsilon_r\right)^{3/2}$ and ε_r is the high frequency (optical) relative dielectric constant. By calculating the slopes of linear least-square fits of the low temperature n_H (~α) allows for an estimation of β using[37] ε_r=5and Z=2 corresponding to singly occupied vacancies. Using this type of analysis we found β=0.2 meV cm$^{1/2}$/V$^{1/2}$ for CMO and β=0.4 meV cm$^{1/2}$/V$^{1/2}$ for SMO.

6.3 Discussion

Although the behavior of fixed temperature individual n_H versus $F^{1/2}$ curves changes for both samples as the temperature increases, all these plots share a common feature: they all extrapolate toward the value of n_H at room temperature. Since n_H(300 K) represents a regime with all the carriers out of their traps and into the conduction band, it follows that all the carriers are bound in Coulomb potentials in the ground state, making a strong argument for the presence of bound magnetic polarons (not self-trapped).

Evident in both resistivity and Hall data is the different magnitude of the field effect in CMO and SMO, consistent with a difference in barrier height δ for the two specimens. If we assume that $N_0 = N_D - N_A = n_H(300K)$, an estimation of δ can be made based on the formula for n_H provided by the Poole-Frenkel model applied to our low temperature data. Such an analysis leads to δ_{CMO}=45 meV and δ_{SMO}=3.5 meV for CMO

and SMO respectively, meaning that the carriers are not excited into the conduction band (which would require energy Δ) but into a band of more mobile states responsible for the low-T conduction.

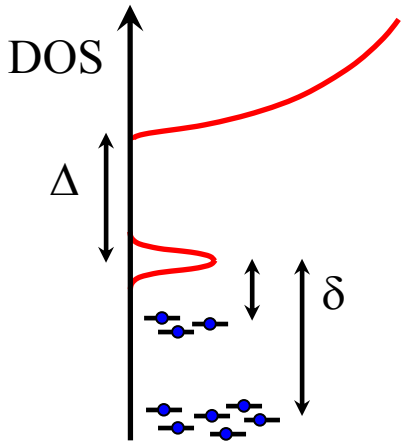

Fig. 6.7 *Energy band scheme*

An analysis similar to the one above but for the higher temperature n_H curves (28, 56 and 100 K for SMO) implies δ~14+3 meV indicating that there is more than one bound state energy (*Fig. 6.7*). That is to be expected since different local environments (associated vacancy clusters or vacancy-acceptor pairs) could cause multiple bound state energies. As the temperature increases we expect that electron with larger binding energies to be thermally activated into this impurity band and rendered mobile in the applied field.

A strong electric field dependence is also exhibited by the Hall mobility. In the higher temperature regime, an abrupt increase in Δn_H for very small transport fields (absent at lower temperatures) is attributed to carriers that are already thermally activated into the impurity band and very low fields are enough to render them mobile. This corresponds to the ohmic regime in σ *(Fig. 6.4)* and implies $\mu_H \sim n_H^{-1}$. At higher fields the values of α found from σ data and the ones from n_H start being quite different (at 4.2K

$\alpha_\sigma \approx 2\alpha_{n_H}$) implying $\mu_H \sim n_H^{-1/2}$. This seems to suggest that within the Poole Frenkel ionization regime, the impurity band carrier mobility is influenced by both magnetic and Coulomb interactions associated with detrapping.

Given the antiferromagnetic alignment of spins in the lattice which inhibits nearest-neighbor hopping (i.e. Hund's rule), it is likely that transport in the impurity band involves next-nearest-neighbor manganese e_g orbitals. This band may involve excited impurity states since the bound electrons are separated by a mean spacing of $\approx 2\left[3/4\pi\left(N_D - N_A\right)\right]^{1/3} \approx 60-80$ Å and radius of 7-11Å, so little overlap, if any, is to be expected.

The results reported here reveal an intriguing interplay between defect states and magnetic polaron formation. A distinction between bound and self trapped magnetic polarons is made possible by a favorable electron configuration. This configuration requires the presence of a mobile band of impurity states to which the electrons, bound at an energy delta below, are excited through barrier lowering in weak electric fields. Such an impurity band derived from states involving oxygen vacancies is likely common to other oxides. This type of measurements can be employed in impurity level spectroscopy and study of correlated electron systems with a tunable mobile carrier density.

Chapter 7

Conclusion and Open Questions

7.1 Thermal Conductivity Studies

Heat conduction studies in antiferromagnetic $RMnO_3$ compounds have been previously reported[49,50] and they all show the same general behavior: the suppression of the thermal conductivity in the paramagnetic phase followed by a sudden revival below T_N (see for example *Ref. [49]*). Although they to not exclude a magnon contribution, Hejtmanek *et al.* attributed this enhancement to a decrease in phonon scattering by spins in the ordered phase (which increases the phonon mean free path) but details about this phonon-spin interactions are unclear. A more complete explanations is offered by Goodenough's study[49]. He associates the suppression of thermal conductivity in the paramagnetic phase of several antiferromagnetic insulators with bond length fluctuations induced by an exchange striction[11] caused mainly by semicovalent exchange interactions. The size of the effect can be quite different throughout $RMnO_3$ class and this variation has been attributed to the fact that some of these systems are at a crossover between localized and delocalized electrons and this enhances the bond length fluctuations induced by magnetostriction[51].

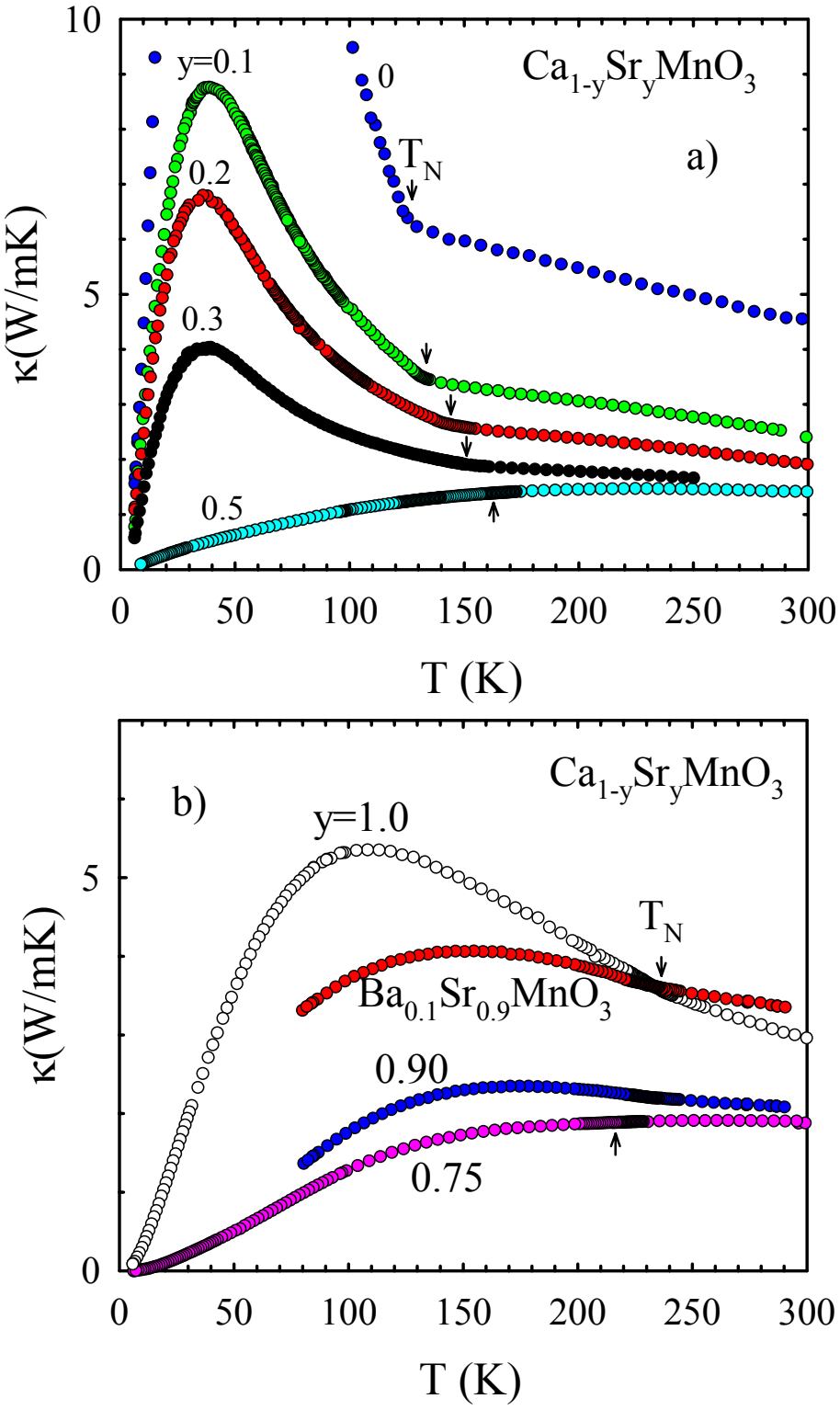

Fig. 7.1 *Thermal conductivity of the $Ca_{1-y}Sr_yMnO_3$ class*

Previously published studies on $Ca_{1-y}Sr_yMnO_3$ show that the Nèel temperature varies linearly with $cos^2\theta$ (Mn-O-Mn bond angle) in the orthorhombic phase[15]. In the same paper, Chmaissem *et. al.* (*Ref. [15]*) show that as y increases, this dependence deviates from linearity and the crystal structure changes abruptly to tetragonal $0.6<y< 0.8$ and becomes cubic for $0.8<y<1$. Whether this change in structure/bond angle can be correlated with the behavior of the thermal conductivity (*Fig. 7.1*) is still an open question. It is interesting to note that a sudden revival of $\kappa(T)$ that occurs at T_N is attributable to a change in scattering with the onset of the magnetic order. In the orthorhombic phase, the peak decreases with increasing Sr content and it appears again as we move into the cubic phase. The much weaker enhancement of $\kappa(T)$ for the cubic compounds (also shown in *Fig. 7.1 b* are two $Ba_{1-y}Sr_yMnO_3$ samples with cubic structure) suggests that exchange strictive fluctuations might not be present in SMO.

Another interesting phenomenon observed in these compounds is the effect of the oxygen deficiency on thermal conductivity, shown in *Fig. 7.2* for the same $CaMnO_3$ single crystal specimen, before and after annealing it in oxygen atmosphere. It can be clearly seen in this plot the change in κ's behavior most probably caused by a change in oxygen stoichiometry. One possible explanation assumes that lattice distortions created by these vacancies are decreased by the smaller vacancy concentration after annealing. The number of phonon scattering centers decreases, effectively lengthening the phonon mean free path and leading to an increase in thermal conductivity. This would imply that a Debye fit function in which only the term responsible for phonon scattering on point like defects could model this effect. Further analysis is required in order to address this issue.

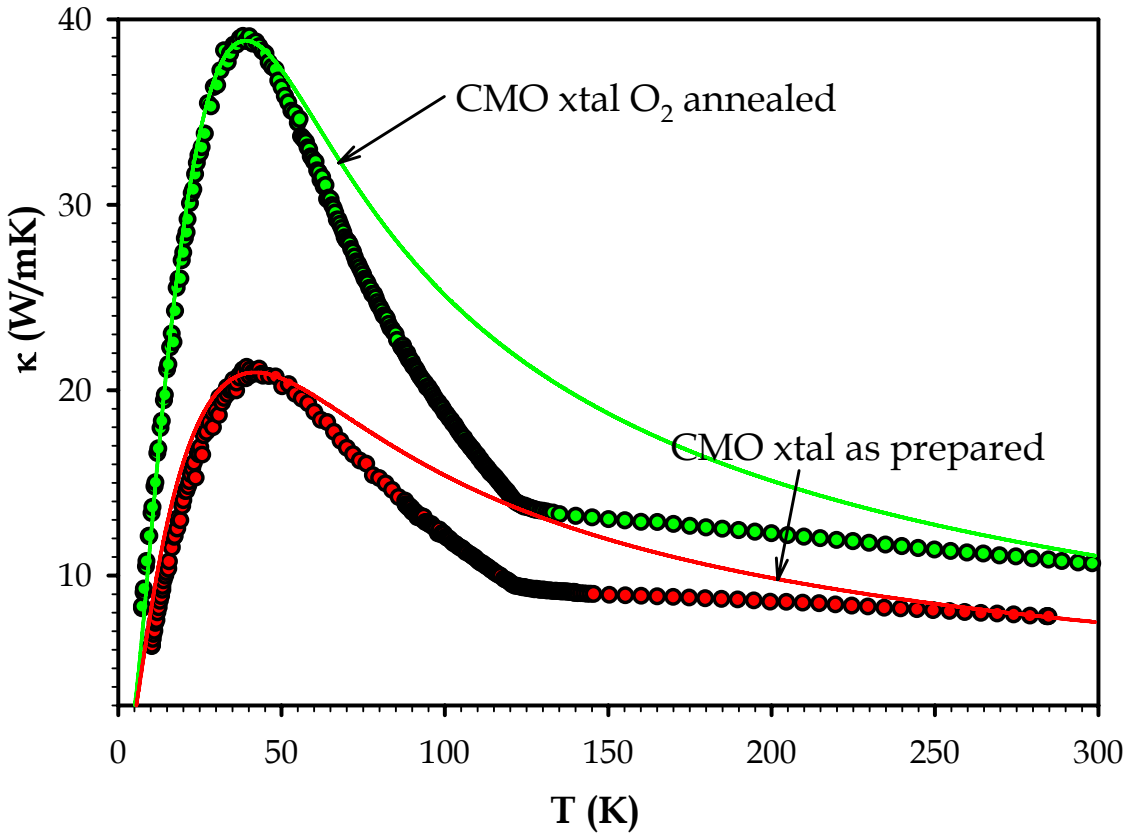

Fig. 7.2 *Thermal conductivity of $CaMnO_3$ single crystal specimen (circles) Debye fits of the data (solid lines)*

The importance of the Poole-Frenkel field assisted ionization of the charge carriers and the way it affects the transport properties of the lightly electron-doped manganese oxides are reflected in a current dependent thermal conductivity for $CaMnO_3$, shown in *Fig. 7.3* for a *polycrystalline specimen*. As the sample current increases from 0 to 0.01 A, the higher current curves start "peeling" off the main curve, an effect very similar to the one presented for the electrical resistivity. Very recent data on a $CaMnO_3$ *monocrystal* shows the same type of behavior but much enhanced in terms of temperature range for which it appears. The difference may be caused by grain boundary scattering

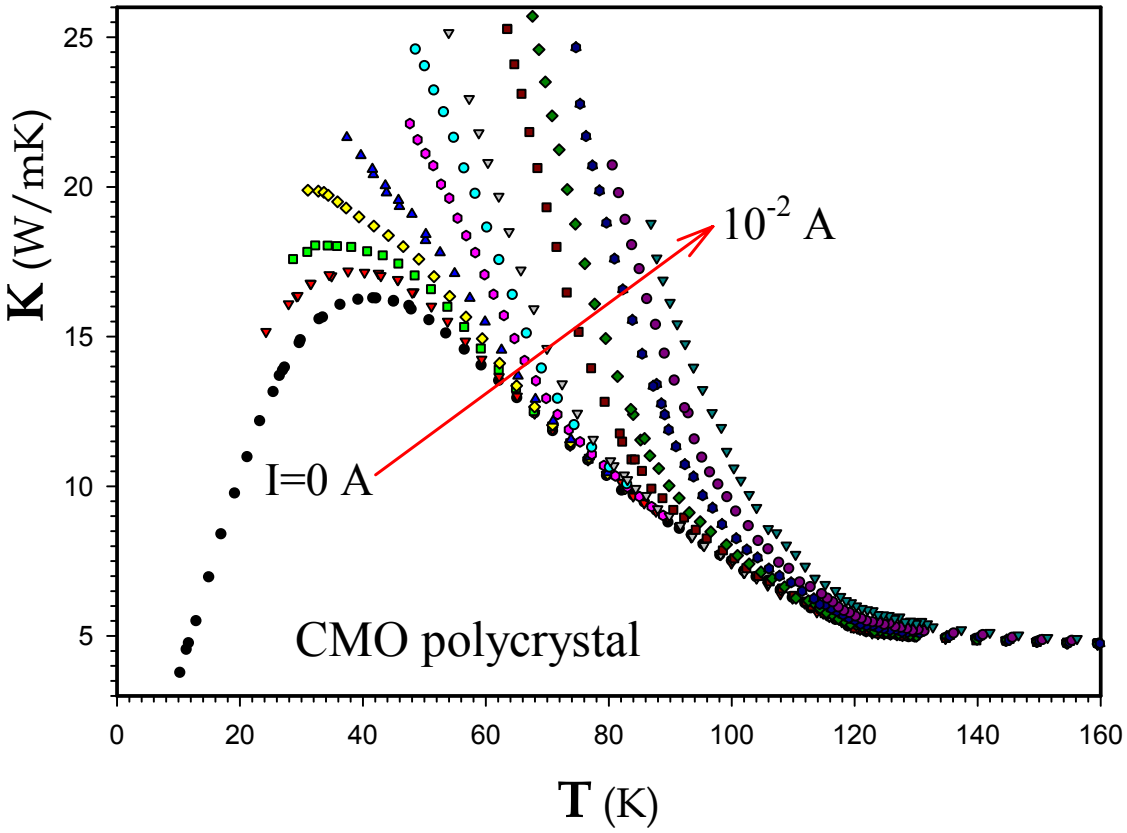

Fig. 7.3 *Thermal conductivity of $CaMnO_3$ polycrystal and its dependence with an external electric field (the black circles represent I=0 curve)*

which masks the true magnitude of the effect.

One thing that is certain is that charge delocalization is responsible for this effect but the exact mechanism is still unclear. It is possible that removing electrons out of their traps effectively removes lattice distortions, removing scattering center for the phonons and thus enhancing κ. However, a preliminary analysis of this picture seems to disagree with this scenario and further work is required in order to explain this effect. The key result is that a very small number of mobilized charge carriers ($\Delta n \sim 10^{-17}$ cm^{-3}~1% of total n) causes a dramatic suppression of phonon scattering.

7.2 Conclusion

It has been shown that, despite their aparent simplicity, the electron doped manganese oxides exhibit a number of very interesting phenomena. While phase segregation is an issue pretty much agreed upon by the scientific community, other questions arise and answering these questions could keep a scientist busy for a while.

In summary, our results on $Ca_{1-x}La_xMnO_3$ sustain the phase separation picture predicted to be a valid description of this system by both theoretical studies and experimental data. A crossover that marks the transition between isolated and interacting ferromagnetic clusters was found at x=0.02. In the paramagnetic phase, it has been found that the small-polaron approach used to describe the CMR compounds is not suitable for the electron-doped side of the phase diagram, where a large, continuum polaron picture in an intermediate coupling regime seems to be more adequate.

Transport studies of $Ca_{1-y}Sr_yMnO_3$ show an intriguing behavior of the resistivity and thermal conductivity: they both depend on the applied transport current. While the Poole-Frenkel field assisted ionization of the charge carriers is successful in describing the resistivity data, further investigation is required in the case of thermal conductivity. Throughout the doping range, the enhancement of κ below the Nèel temperature is caused by the onset of the magnetic order. Its suppression in the paramagnetic phase is attributed to Mn-O-Mn bond length fluctuations induced by exchange striction.

References

[1] Bednorz, J. G. & Müller, K. A. *Z. Phys. B* **64**, 189-193 (1986)

[2] R. von Helmolt, J. Wecker, B. Holzapfel, L. Schultz, and K. Samwer, Phys. Rev. Lett. **71**, 2331 - 2333 (1993)

[3] G. H. Jonker and J. H. van Santen, Physics (Utrecht) **16**, 337 (1950)

[4] S.-W. Cheong and H. Y. Hwang: *Ferrromagnetism vs Charge/Orbital Ordering in Mixed-Valent Manganites,* in *Colossal Magnetoresistance Oxides*, edited by Y. Tokura (Gordon & Breach, Monographs in Condensed Matter Science, London, 1999)

[5] Y. Tokura and N. Nagaosa, Science **288**, 462 (2000)

[6] E. Dagotto, *Nanoscale Phase Separation and Colossal Magnetoresistance* (Springer, Berlin, 2002)

[7] C. Zener, Phys. Rev. **81**, 440 (1951)

[8] P.W. Anderson and H. Hasegawa, Phys. Rev. **100**, 675 (1955)

[9] P.-G. de Gennes, Phys. Rev. **118**, 141 (1960)

[10] John B. Goodenough, Phys. Rev. **100**, 564 (1955)

[11] John B. Goodenough, *Magnetism and the Chemical Bond* (Interscience, New York, 1963)

[12] J. J. Neumeier and J. L. Cohn, Phys. Rev. B **61**, 14319 (2000)

[13] C.D. Ling *et al.*, Phys. Rev. B **68** 134439/1-8 (2003)

[14] E. Granado *et al.*, Phys. Rev. B **68** 134440/1-6 (2003)

[15] O. Chmaissem *et al*, Phys. Rev. B **64**, 134412 (2001)

[16] R. Berman, *Thermal Conduction in Solids* (Clarendon Press, Oxford, 1976)

[17] J. L. Cohn, C. Chiorescu and J. J. Neumeier, Phys. Rev. B **72**, 024422 (2005)

[18] E. T. Swartz, Rev. Sci. Instrum. **58**, 881 (1987)

[19] M. Hennion, *et al*., Phys. Rev. Lett. **81**, 1957 (1998); M. Hennion, *et. al.* Phys. Rev. B **61**, 9513 (2000)

[20] H. Terashita and J. J. Neumeier, Phys. Rev. B **71**, 134402 (2005)

[21] E. Granado, *et al*., Phys. Rev. Lett. **86**, 5385 (2001); Aliaga, *et al*., cond-mat/0010295 (unpublished); C. Martin *et al.*, Phys. Rev. B **62**, 6442 (2000)

[22] P. Majumdar and P. B. Littlewood, Nature **395**, 479 (1998)

[23] H. Aliaga, M. T. Causa, M. Tovar, and B. Alascio, Physica B **320**, 75 (2002)

[24] Terry M. Tritt and David Weston, *Measurement Techniques and Considerations for Determining Thermal Conductivity of Bulk Materials,* in *Thermal Conductivity – Theory, Properties and Applications*, edited by Terry M. Tritt (Kluwer Academic / Plenum Publishers, New York, 2004), p. 191

[25] A. Urushibara, *et al.,* Phys. Rev. B **51**, 14103 (1995); M. F. Hundley, *et al*., Appl. Phys. Lett. **67**, 860 (1995); B. Martinez, *et al*., Phys. Rev. B **54**, 10001 (1996); Y. Tomioka, *et al*., *ibid.* **63**, 024421 (2001)

[26] Y.-R. Chen and P. B. Allen, Phys. Rev. B **64**, 064401 (2001)

[27] H . Meskine, T. Saha-Dasgupta, and S. Satpathy, Phys. Rev. Lett. **92**, 056401 (2004)

[28] Y.-R. Chen and P. B. Allen, Phys. Rev. B **64**, 064401 (2001)

[29] M. Jaime, H. T. Hardner, M. B. Salamon, M. Rubinstein, P. Dorsey, and D. Emin, Phys. Rev. Lett. **78**, 951 (1997); J. L. Cohn, J. Supercond. **13**, 291 (2000); M. B. Salamon and M. Jaime, Rev. Mod. Phys. **73**, 583 (2001)

[30] C. Chiorescu, J. L. Cohn and J. J. Neumeier, Phys. Rev. B **73**, 014406 (2006)

[31] A. Maignan, C. Martin, F. Damay, B. Raveau, and J. Hejtmánek, Phys. Rev. B **58**, 2758 (1998)

[32] C. Martin, *et al.,* Phys. Rev. B **62**, 6442 (2000); M. M. Savosta *et al., ibid.* **62**, 9532 (2000)

[33] H. Aliaga, M. T. Causa, M. Tovar, and B. Alascio, Physica B **320**, 75 (2002); H. Aliaga, M. T. Causa, B. Alascio, H. Salva, M. Tovar, D. Vega, G. Polla, G. Leyva, and P. Konig, J. Magn. Magn. Mater. **226–230**, 791 (2001)

[34] Ting-Kang Xia and D. Stroud, Phys. Rev. B **37**, 118 (1988)

[35] G. A. Slack and M. H. Hussain, J. Appl. Phys. **70**, 2694 (1991)

[36] J. L. Cohn, M. Peterca, and J. J. Neumeier, Phys. Rev. B **70**, 214433 (2004)

[37] A. S. Alexandrov and A. M. Bratkovsky, J. Phys.: Condens. Matter **11**, L531 (1999)

[38] K. Seeger, *Semiconductor Physics* (Springer-Verlag, Berlin, 1997)

[39] R. P. Feynman, Phys. Rev. **97**, 660 (1955); R. P. Feynman, R. W. Hellwarth, C. K. Iddings, and P. M. Platzman, *ibid.* **127**, 1004 (1962)

[40] R. W. Hellwarth and I. Biaggio, Phys. Rev. B **60**, 299 (1999)

[41] D. Chattopadhyay and H. J. Queisser, Rev. Mod. Phys. **53**, 745 (1981)

[42] D. J. Howarth and E. H. Sondheimer, Proc. R. Soc. London, Ser. A **219**, 53 (1953)

[43] E. L. Nagaev, Zh. Eksp. Teor. Fiz. Pis'ma Red. **6**, 484 (1967); T. Kasuya, A. Yanase, and T. Takeda, Solid State Commun. **8**, 1543 (1970); A. Mauger and D. L. Mills, Phys. Rev. B **31**, 8024 (1985); L. Liu, Phys. Rev. B **37**, 5387 (1988)

[44] I. Dzyaloshinsky, J. Phys. Chem. Solids **4**, 241 (1958)

[45] T. Moryia, Phys. Rev. **120**, 91 (1960)

[46] C. Chiorescu, J. L. Cohn and J. J. Neumeier, Phys Rev. B **76**, 020404(R)/1-4 (2007)

[47] J. Smit, Physica **24**, 39 (1958)

[48] R. Karplus, J. M. Luttinger, Phys. Rev. ***95***, 1154 (1954)

[49] J.-S. Zhou and J. B. Goodenough, Phys. Rev. B **66**, 052401 (2002)

[50] J. Hejtmanek *et al.*, Phys. Rev. B **60**, 14057 (1999)

[51] J.-S. Zhou and J. B. Goodenough, Phys. Rev. B **68**, 054403 (2003); L. Kebin *et al.*, J. Appl. Phys. **81**, 6943 (1997); M. V. Abrashev *et al.*, Phys. Rev. B **65**, 184301 (2002); L. Martín-Carrón *et al.*, *ibid.* **66**, 174303 (2002); N. N. Loshkareva *et al. ibid.* **70**, 224406 (2004)